

1 **A Middle Crustal Channel of Radial Anisotropy Beneath the Northeastern Basin and**
2 **Range**

3
4 Justin Wilgus¹, Chengxin Jiang^{1*}, Brandon Schmandt¹

5 1. Department of Earth and Planetary Sciences, University of New Mexico, Albuquerque, NM, USA

6 *now at Research School of Earth Sciences, The Australian National University, Acton, ACT, Australia

7
8 Corresponding author: Justin Wilgus (jwilgus@unm.edu)
9

10 **Key Points**

- 11 ● Evidence for a channel of positive radial anisotropy with peak magnitude at depths of ~8-
12 20 km throughout the study area
- 13 ● Absence of locally distinctive deep crustal V_S beneath core complexes suggests over-
14 printing by middle Miocene regional ductile extension
- 15 ● Diminished anisotropy in the hotter lowermost crust may result from decreased mica
16 abundance and a transition to more distributed strain

17
18
19
20
21
22
23
24
25
26
27
28
29
30
31
32
33
34
35
36
37
38

39 **Abstract**

40 A challenge in interpreting the origins of seismic anisotropy in deformed continental crust is that
41 composition and rheology vary with depth. We investigated anisotropy in the northeastern Basin
42 and Range where prior studies found prevalent depth-averaged positive radial anisotropy ($V_{SH} >$
43 V_{SV}). This study focuses on depth-dependence of anisotropy and potentially distinct structures
44 beneath three metamorphic core complexes (MCC's). Rayleigh and Love wave dispersion were
45 measured using ambient noise interferometry and Bayesian Markov Chain Monte Carlo
46 inversions for V_S structure were tested with several (an)isotropic parameterizations. Acceptable
47 data fits with minimal introduction of anisotropy are achieved by models with anisotropy
48 concentrated in the middle crust. The peak magnitude of anisotropy from the mean of the
49 posterior distributions ranges from 3.5-5% and is concentrated at 8-20 km depth. Synthetic tests
50 with one uniform layer of anisotropy best reproduce the regional mean results with 9%
51 anisotropy at 6-22 km depth. Both magnitudes are feasible based on exhumed middle crustal
52 rocks. The three MCC's exhibit ~5% higher isotropic upper crustal V_S , likely due to their
53 anomalous levels of exhumation, but no distinctive (an)isotropic structures at deeper depths.
54 Regionally pervasive middle crustal positive radial anisotropy is interpreted as a result of sub-
55 horizontal foliation of mica-bearing rocks deformed near the top of the ductile deformation
56 regime. Decreasing mica content with depth and more broadly distributed deformation at lower
57 stress levels may explain diminished lower crustal anisotropy. Absence of distinctive deep
58 crustal V_S beneath the MCC's suggests over-printing by ductile deformation since the middle
59 Miocene.

60

61 **Plain Language Summary**

62 The northeastern Basin and Range is an area of Earth's crust that has been dramatically stretched
63 and thinned by tectonic forces. Seismic anisotropy, or wave speed dependence on direction, can
64 provide useful insights into the way in which such deformation organizes crustal structure over
65 long periods of time. We used surface waves to identify discrepancies between horizontally and
66 vertically polarized wave speeds. Anisotropy focused in the middle crust at ~8-20 km is found to
67 best resolve the observed discrepancies. The results suggest that development and preservation
68 of anisotropy is more effective in the middle crust compared to the lowermost crust. The
69 transition with depth may be explained by increasingly high temperature in the lowermost crust
70 that reduces the abundance of highly anisotropy mica minerals and promotes ductile flow that is
71 distributed across larger volumes rather than localized shear zones. Additionally, we find that
72 areas of exceptionally localized extension called metamorphic core complexes have middle-to-
73 lower crustal seismic structure that is similar to the surrounding region despite their distinctive
74 upper crustal structure. These structures formed early in the development of the Basin and
75 Range, consequently we suggest that subsequent ductile deformation in the middle-to-lower crust
76 largely over-printed their structural legacies.

77

78 **1. Introduction**

79 The central-to-northern Basin and Range province of the western U.S. Cordillera is an area of
80 large magnitude extensional strain, with up to ~100% regional-scale crustal extension since the
81 Eocene (Hamilton and Myers, 1966; Wernicke et al., 1988; McQuarrie and Wernicke, 2005;
82 Colgan and Henry, 2009; Long, 2018). Embedded within this region of distributed deformation
83 are localized zones of more extreme extension and exhumation recorded in metamorphic core
84 complexes (MCC), which expose rocks that were deformed below the brittle-ductile transition
85 and exhumed during the development of the Basin and Range (e.g., Crittenden et al., 1980;
86 Whitney et al., 2013; Platt et al., 2015). Regional-scale extensional strain rate peaked in the
87 middle Miocene (McQuarrie and Wernicke, 2005; Colgan and Henry, 2009). Slower but ongoing
88 right-lateral transtensional deformation is identified by geodetic studies, with ~1 cm/year
89 northwest-directed relative motion between the low-strain crustal blocks of the Sierra Nevada
90 and Colorado Plateau located on either side of the central-to-northern Basin and Range (Bennett
91 et al., 2003; Hammond and Thatcher, 2004). As a result of the well-constrained deformation over
92 geological and contemporary time scales, the Basin and Range and its internal MCC's are useful
93 places to study potential indicators of how subsurface strain is organized, such as seismic
94 anisotropy.

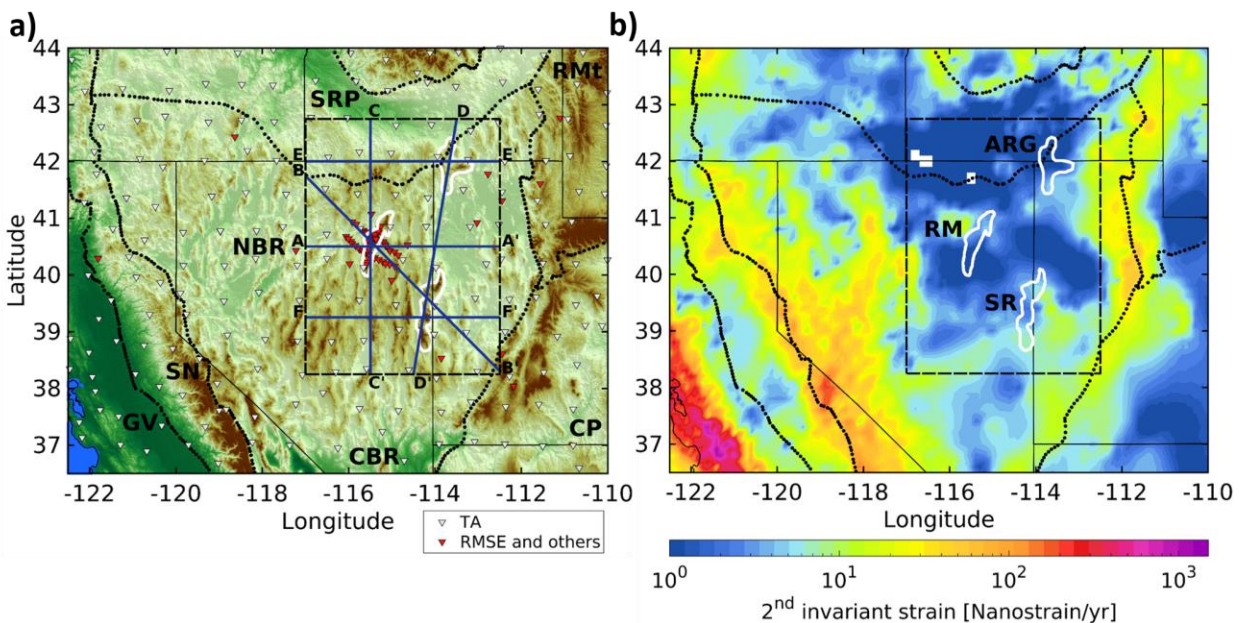
95 In this study, we investigate links between deformation recorded at the surface and the
96 development of radial seismic anisotropy in extended continental crust. We focus on the
97 northeastern Basin and Range surrounding three MCC's: the Ruby Mountains, Snake Range, and
98 Albion-Raft River-Grouse Creek (Fig. 1). The distribution of crustal anisotropy is a subject of
99 expanded investigation in recent years, in part due to the development of seismic noise
100 interferometry methods that enable extraction of short-period surface wave measurements
101 between pairs of seismographs (e.g., Shapiro and Campillo, 2004; Sabra et al., 2005). Inter-
102 station noise interferometry is powerful for crustal imaging with dense and large aperture seismic
103 arrays like the Transportable Array (TA) component of EarthScope's USArray, which provides
104 excellent geographic distributions of short-period Rayleigh and Love wave paths compared to
105 relying on earthquakes (e.g., Lin et al., 2008). This study focuses on radial anisotropy, which
106 makes the simplifying assumption of transverse isotropy with a vertical symmetry axis to explain
107 inconsistencies between Rayleigh and Love wave dispersion with independent horizontally and
108 vertically polarized V_S , referred to as V_{SH} and V_{SV} (Babuska and Cara, 1991).

109 Prior investigation of radial anisotropy beneath the Basin and Range used TA data to find
110 that positive radial anisotropy ($V_{SH} > V_{SV}$) is prevalent in the crust and correlated with areas of
111 extensional deformation (Moschetti et al., 2010a,b). Crustal radial anisotropy has been detected
112 in other parts of the North American Cordillera including the southern California transform
113 margin (Wang et al., 2018), the Rio Grande rift (Fu and Li, 2015), the Canadian Rockies (Dalton
114 and Gaherty, 2013), and Alaska (Feng and Ritzwoller, 2019). Globally, crustal radial anisotropy
115 has been identified in many continental areas including tectonically active and cratonic settings
116 (e.g., Shapiro et al., 2004; Sherrington et al., 2004; Huang et al., 2010; Duret et al., 2010; Xie et
117 al., 2013; Luo et al., 2013; Cheng et al., 2013; Harmon and Rychert, 2015; Dreiling et al., 2018;

118 Ojo et al., 2017; Lynner et al., 2018). The most conventional interpretation for its origin is the
 119 strain-induced alignment of anisotropic crustal minerals forming an aggregate crystallographic
 120 preferred orientation (CPO; Mainprice and Nicolas, 1989; Weiss et al., 1999). However, there
 121 are plausible alternatives or additional contributions such as preferentially oriented fractures in
 122 the shallow crust, sedimentary stratigraphy, and organization of partial melt or fluids that may be
 123 prevalent in thick orogenic crust or magmatic systems (e.g., Leary et al., 1990; Backus, 1962;
 124 Hacker et al., 2014; Matharu et al., 2014; Almqvist and Mainprice, 2017; Harmon and Rychert,
 125 2015; Jaxybulatov et al., 2014; Jiang et al., 2018; Lynner et al., 2018). The thin crust of the
 126 modern Basin and Range makes pervasive mid-crustal melting less likely compared to settings
 127 such as the Tibetan plateau, which has about double the thickness of radiogenic heat-producing
 128 crust (e.g., Hacker et al., 2014). Moschetti et al. (2010a) favor CPO as the most probable origin
 129 of radial anisotropy in the highly extended middle and lower crust of the Basin and Range, and
 130 laboratory measurements of exhumed rocks from the Basin and Range support the presence of
 131 CPO-derived anisotropy and the approximate validity of transverse isotropy (Erdman et al.,
 132 2013).

133 We further investigate radial anisotropy in the northeastern Basin and Range with
 134 combined analysis of Rayleigh and Love waves extracted from TA data and a denser regional
 135 array centered on the Ruby Mountains MCC (Fig. 1). Prior investigations using only the TA
 136 lacked the seismograph density to identify potentially anomalous anisotropy beneath Ruby
 137 Mountains MCC and focused on establishing the necessity of regionally prevalent anisotropy by
 138 assuming a uniform distribution in the middle and lower crust (Moschetti et al., 2010a). This
 139 study evaluates whether distinctive radial anisotropy exists beneath the Ruby Mountains or other
 140 MCC's in the northeastern Basin and Range. We also evaluate depth dependence of radial
 141 anisotropy to identify how depth-dependent composition and rheology may influence
 142 development of crustal radial anisotropy.

143



144

145 **Figure 1.** Maps of seismic data coverage and active regional deformation. (a) Broadband seismographs used for
146 ambient noise cross correlations including the RMSE (red) and Transportable Array (TA) stations (white) used in
147 the USANT model. Black dotted lines define geologic provinces from Fenneman, (1917): Colorado Plateau (CP),
148 Great Valley (GV), northern Basin and Range (northern Basin and Range), central Basin and Range (CBR), Rocky
149 Mountains (RMt), Sierra Nevada (SN), Snake River Plain (SRP). Black dashes delineate the focus area used in
150 subsequent figures. Solid blue lines delineate surface trace of cross sections shown in Fig. 7. (b) Regional second
151 invariant of strain rate estimated from inversion of GPS measurements (Kreemer et al., 2014). White outlines show
152 metamorphic core complexes of the northern Basin and Range: Albion-Raft River-Grouse Creek (ARG), Ruby
153 Mountains-East Humboldt (RM), Snake Range (SR).

154

155 **2. Geologic and geodynamic setting**

156 Formation of the Basin and Range as a province of extensional deformation and intraplate
157 magmatism began in the Paleogene and closely followed cessation of Mesozoic crustal
158 shortening that culminated with the Sevier and Laramide orogenies (Coney and Harms, 1984).
159 Western plate boundary re-organization including subduction of the Kula-Farallon and Pacific-
160 Farallon ridges decreased subduction zone width and coincided with the transition from
161 dominantly compressional to extensional deformation in the Cordilleran interior (Schellart et al.,
162 2010). Diminished compressional stress and thick elevated continental crust gave rise to
163 gravitational collapse in what became the Basin and Range (Coney and Harms, 1984; Dewey,
164 1988; Rey et al., 2001). Post-orogenic collapse began with voluminous magmatism and localized
165 extension sweeping from north to south in the Eocene and Oligocene, while regional scale
166 extension dominantly occurred in the middle Miocene (Best and Christiansen, 1991; Wernicke
167 and Snow, 1998; Colgan and Henry, 2009; Camp et al., 2015). Columbia River, Steens, and
168 northern Nevada Rift basaltic volcanism (~15-17 Ma) were approximately coeval with Miocene
169 acceleration of extension in the northern Basin and Range, suggesting that mantle upwelling
170 further contributed to driving extensional collapse (Colgan and Henry, 2009; Camp et al., 2015).
171 Continued growth of the San Andreas transform boundary since ~10 Ma was accompanied by an
172 increasing component of right-lateral shear strain and concentration of strain near the boundaries
173 of the Basin and Range compared to its interior (Wernicke and Snow, 1998; Colgan and Henry,
174 2009). Slow contemporary strain rates (Fig. 1; Bennett et al., 2003; Hammond and Thatcher,
175 2004; Kreemer et al., 2014) are consistent with minor amounts of slip on extensional faults in the
176 north-central Basin and Range from the late Miocene through the Holocene (Pérouse and
177 Wernicke, 2017).

178 Within the northern Basin and Range are three MCCs: the Ruby Mountains-East
179 Humboldt Range, Snake Range, and Albion-Raft River-Grouse Creek Mountains (Fig. 1). This
180 study benefits from data collected by the recent Ruby Mountains Seismic Experiment (RMSE),
181 which provides exceptionally dense, ~5-10 km spacing, broadband seismograph coverage of the
182 Ruby Mountains (Fig. 1; Litherland and Klemperer, 2017). The northern Ruby Mountains
183 expose Proterozoic to Paleozoic metasedimentary rocks of the miogeocline that were intruded by
184 Mesozoic to early Cenozoic plutons, buried during crustal shortening of the Sevier Orogeny, and
185 then subjected to multiple phases of exhumation beginning in the late Cretaceous (Hodges et al.,
186 1992; MacCready et al., 1997; Sullivan and Snoke, 2007). The southern Ruby Mountains expose

187 unmetamorphosed Paleozoic sedimentary rocks that have not been buried below their
188 stratigraphic depths (Colgan et al., 2010). Intrusion of the Harrison Pass pluton into the transition
189 between the southern and northern Ruby Mountains occurred at ~36 Ma during an Eocene to
190 Oligocene period of ductile shear deformation in the middle crust (Barnes et al., 2001;
191 MacCready et al., 1997). Exhumation and extension in the southern Ruby Mountains were
192 concentrated in the middle Miocene from ~17-10 Ma (Colgan et al., 2010; Haines and van der
193 Pluijm, 2010).

194 The Snake Range and Albion-Raft River-Grouse Creek (ARG) MCCs are included in the
195 study area, but data coverage in these regions are mainly provided by the TA seismographs
196 spaced ~70 km apart (Fig. 1, Supplementary Information S1, T1). The Snake Range MCC
197 exposes Proterozoic to Cenozoic strata and records up to ~450% extension of the brittle upper
198 crust (Lee et al., 1987). Metamorphism and ductile deformation of the deeply exhumed footwall
199 dominantly occurred from the Oligocene to early Miocene, ~35-20 Ma, followed by fault-driven
200 exhumation to within ~3 km of the surface in the middle Miocene, ~17 Ma (Miller et al., 1999;
201 Gébelin et al., 2011). In the ARG, outcrops expose Archean to Cenozoic stratigraphic units
202 (Compton et al., 1977), and metamorphism of gneiss domes there dominantly occurred in the
203 Oligocene, ~34-25 Ma (Egger et al., 2003; Konstantinou et al., 2013). The ARG exposes strata
204 exhumed from ~10 km greater depth than in the surrounding region, however much of the
205 exhumation was likely driven by locally pronounced thermal weakening of the crust and ascent
206 of granitic diapirs during the Oligocene (Konstantinou et al., 2013). A later phase of fault-driven
207 Miocene exhumation from ~15-7 Ma led to the surface exposures of the ARG MCC (Wells et al.,
208 2000; Egger et al., 2003).

209 Modern lithospheric structure of the northern Basin and Range is characterized by high
210 heat flow, thin continental mantle lithosphere, and a low-relief Moho interface defining an
211 average crustal thickness of ~30-35 km (Hasterok and Chapman, 2007; Klemperer et al., 1986;
212 Zandt et al., 1995; Lowry and Pérez-Gussinyé, 2011; Gilbert et al., 2012; Schmandt et al., 2015).
213 Contemporary heat flow in the northern Basin and Range has an estimated median of 79 mW/m²,
214 which is consistent with steady-state thermal lithospheric thickness of ~75 km (Hasterok and
215 Chapman, 2007). Teleseismic imaging with P-to-S and S-to-P converted waves indicates a sharp
216 lithosphere-asthenosphere boundary at similar or shallower depths of ~55-75 km, and the
217 sharpness and amplitude of the interface, along with temperature estimates from seismic
218 tomography, suggest it may be defined by partial melt at the base of the lithosphere (Levander
219 and Miller, 2012; Lekić and Fischer, 2014; Hansen et al., 2015). Controlled source seismic
220 reflection studies show steeply dipping normal faults in the upper crust, ≤6-8 km, transitioning
221 to prevalent sub-horizontal layering in the middle and lower crust underlain by lower reflectivity
222 mantle lithosphere (e.g., Klemperer et al., 1986; McCarthy, 1986; Hauser et al., 1987; Holbrook
223 et al., 1991; Stoerzel and Smithson, 1998). Fine-scale deep crustal layering illuminated by high
224 frequency reflections may be due to a combination of ductile extension accommodated by
225 localized shear zones and intrusion of mafic sills during the late Eocene through Miocene
226 magmatic flare-up in the Basin and Range (Klemperer et al., 1986; Gans, 1987; McCarthy and

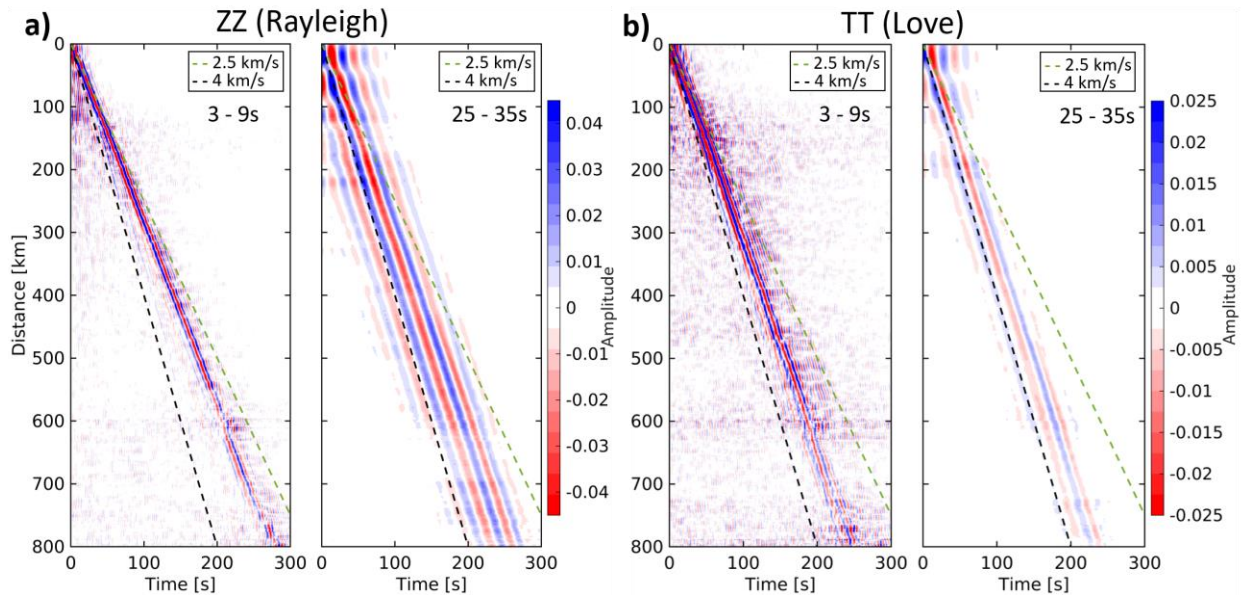
227 Thompson, 1988; Valasek et al., 1989; Holbrook et al., 1991). Regional ductile flow in the
 228 middle-to-lower crust during and after the middle Miocene phase of regional extension is likely
 229 based on the low-relief Moho surface, estimated modern Moho temperatures of ~600-800 °C,
 230 and decoupling of azimuthal anisotropy in the crust and mantle (Klemperer et al., 1986; Gans,
 231 1987; Block and Royden, 1990; Schutt et al., 2018; Lin et al., 2011).

232

233 3. Data and Methods

234 3.1 Data

235 Continuous three-component (3-C) broadband seismic data were collected from the RMSE
 236 (Litherland and Klemperer, 2017) and surrounding permanent network stations (Fig. 1;
 237 Supplementary Information T1). Using inter-station measurements of surface wave propagation
 238 extracted from empirical Green’s functions estimated using ambient noise interferometry we
 239 obtain Rayleigh and Love wave data (Fig. 2; Bensen et al., 2007). Prior to the RMSE the TA,
 240 deployed from ~2006–2008, provided the best broadband coverage of the study area in the
 241 northern Basin and Range with ~70 km spacing. The RMSE deployed 50 3-C broadband
 242 seismometers ~5–10 km apart along three transects across the Ruby Mountains between 2010–
 243 2012, thereby providing opportunities for improved resolution of regional crustal structure.



244

245 **Figure 2.** Stacked noise correlations from the RMSE and regional seismographs. (a) Stacked time versus distance
 246 image of 3260 vertical component (ZZ) inter-station noise cross correlations recorded over ~18 months for the
 247 RMSE and exterior stations (red triangles in Figure 1). Correlations bandpass filtered between 3-9 s and 25-35 s
 248 period are shown in the left and right panels, respectively. Longer periods propagate at higher velocities as expected
 249 for dispersive Rayleigh waves. (b) same as (a), but TT component correlations are plotted to show Love waves.

250 3.2 Phase velocities

251 Inter-station Rayleigh and Love wave dispersion measurements from two different time periods
252 were used to invert for radially anisotropic V_S structure. Rayleigh and Love wave dispersion
253 measurements were made with the vertical (ZZ) and transverse (TT) noise cross-correlation
254 functions, respectively (Fig. 2). Inter-station dispersion measurements from Ekström, (2017)
255 were used for the TA time period 2005-2008. New noise cross-correlations functions were
256 calculated for the RMSE deployment from 2010-2012 (Fig. 2). To better merge the RMSE and
257 TA time period measurements, inter-station noise cross-correlation functions were calculated for
258 the RMSE and a set of 26 azimuthally distributed permanent seismographs operating between
259 2010-2012 (Fig. 1 and Supplementary Information S1). We followed Bensen et al., (2007) to
260 process the new noise cross-correlation measurements, with the slight modification of using half-
261 overlapping 4-hour, rather than daily, time windows (e.g., Seats et al., 2012). Rayleigh and Love
262 wave phase velocities were estimated at 5-30 s periods using frequency-time analysis (Bensen et
263 al., 2007; Lin et al., 2008). Phase velocities from Ekström, (2017) were calculated using Aki's
264 spectral formulation (Ekström et al., 2009), which produces results that are consistent with
265 frequency-time analysis (Tsai and Moschetti, 2010). Three types of quality control were applied
266 to the new dispersion measurements to ensure that: Rayleigh or Love wave signal-to-noise ratio
267 is >6 , phase velocity is between 2-5 km/s, and the inter-station distance is >2 wavelengths. Inter-
268 station phase velocities were inverted for phase velocity maps for periods at 5-30 s for Rayleigh
269 waves and 6-30 s for Love waves using a damped least-squares inversion and great circle ray
270 paths following Ekström, (2017). RMSE measurements with misfits beyond 2 standard
271 deviations were removed and the inversion was repeated once more (Supplementary Information
272 S2).

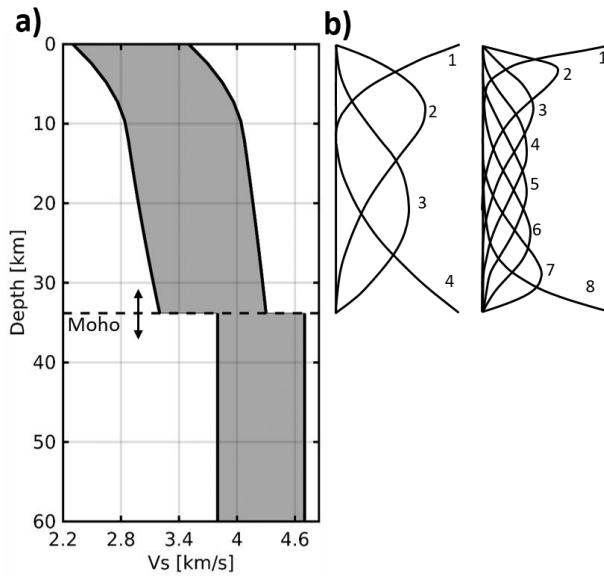
273 3.3 Anisotropic V_S inversion

274 Models of V_S structure as a function of depth were estimated at each geographic location using a
275 Bayesian Markov chain Monte Carlo (BMCMC) inversion (Shen et al., 2012). Each V_S model is
276 parameterized by a set of spline functions in the crust and a single layer in the upper mantle, and
277 the number of splines in the crust and the assumption of isotropy or radial anisotropy were varied
278 in different inversion cases described below (Fig. 3; Supplementary Information S3). Uniform
279 prior distributions were assumed for the values of the spline coefficients. The range of V_S models
280 permitted by the prior distribution is shown in Figure 3. Forward calculations of Rayleigh and
281 Love dispersion curves were performed using the Computer Programs in Seismology software
282 package (Herrmann, 2013). V_P and density needed for forward modelling were derived from the
283 empirical scaling relationships of Brocher, (2005) for the crust. In the upper mantle, we use
284 relative scalings from Panning & Romanowicz, (2006) based on the PREM model. Goodness of
285 fit between predicted and observed dispersion curves was calculated with a standard chi-squared
286 (χ^2) misfit, $\chi^2 = \sum((\text{obs} - \text{pred})^2 / \sigma^2)$, using phase velocity uncertainties, σ , (Supplementary
287 Information T2) from Jiang et al., (2018). Each 1D inversion was run for 1.5 million iterations
288 and model selection is guided by the Metropolis - Hastings algorithm (Hastings, 1970;

289 Mosegaard and Tarantola, 1995). Because the χ^2 values of the best models vary spatially within
 290 the study area, the best 800 models are chosen to represent the posterior distribution. The mean
 291 of the posterior distribution at each geographic point is shown as the final result on a regular
 292 0.25° grid.

293 To validate the necessity of seismic anisotropy in the crust and test the depth-dependence
 294 of radial anisotropy we constructed five different BMMC inversion parameterizations (Fig. 4).
 295 The five cases are: 1) isotropic crust (4 splines) and mantle; 2) isotropic crust (4 splines),
 296 anisotropic mantle; 3) isotropic crust (8 splines), anisotropic mantle; 4) anisotropic crust (4
 297 splines), anisotropic mantle; 5) anisotropic middle crust (middle 2 of 4 splines), anisotropic
 298 mantle (Figs. 3 and 4). In each case the upper mantle layer extends to 100 km depth. PREM
 299 V_p/V_s and density are assumed at depths greater than the local Moho (Dziewonski and
 300 Anderson, 1981). Given the maximum period of 30 s used in this study, there is negligible
 301 sensitivity to structure at >100 km depth. V_{SH} and V_{SV} are independent in inversion cases that
 302 consider anisotropy. The resulting isotropic V_S models were estimated using Voigt averaging, V_S
 303 $= \sqrt{((2V_{SV}^2 + V_{SH}^2) / 3)}$ and radial anisotropy was calculated post-inversion where, radial
 304 anisotropy $= 100(V_{SH} - V_{SV}) / V_S$.

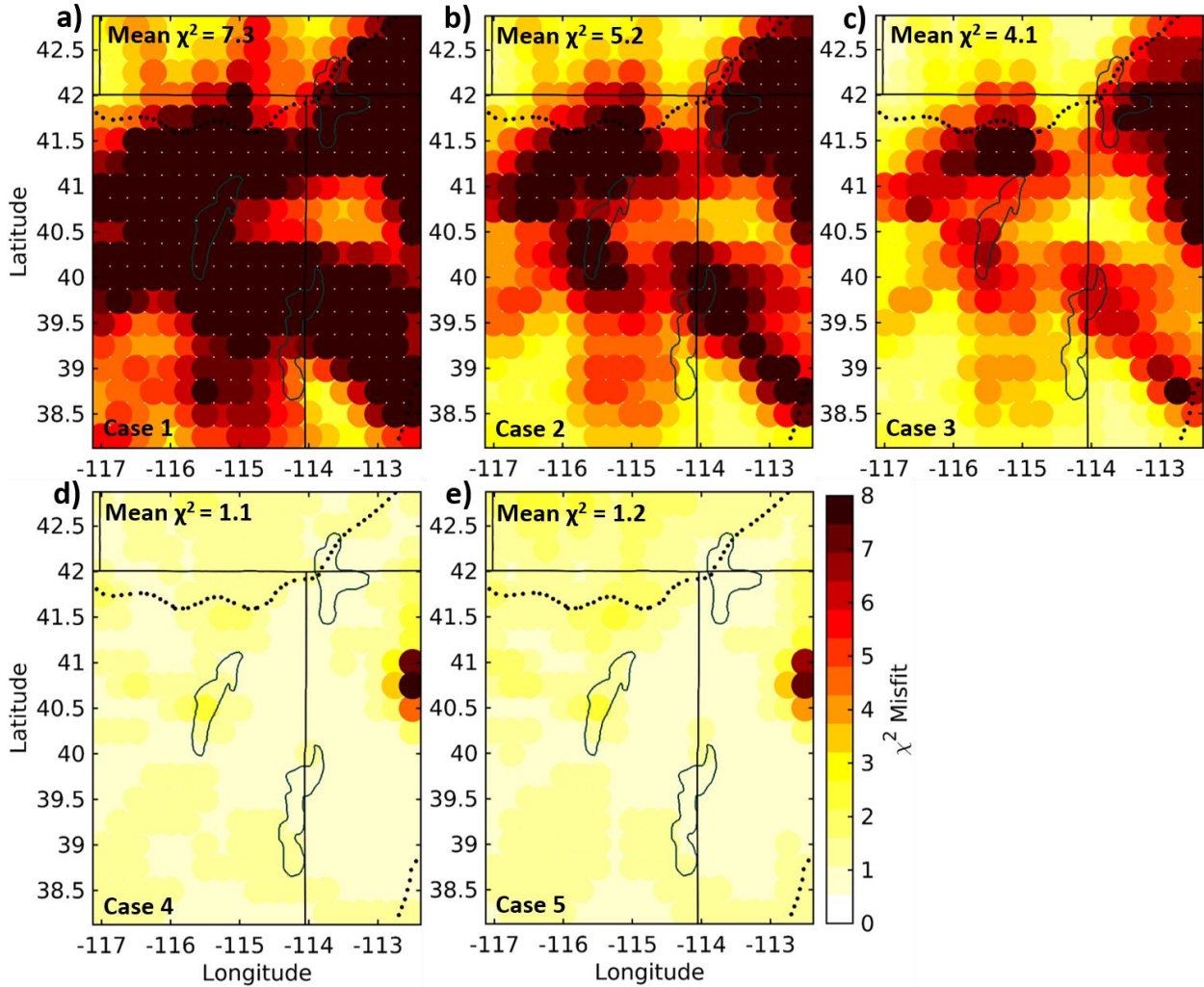
305



306

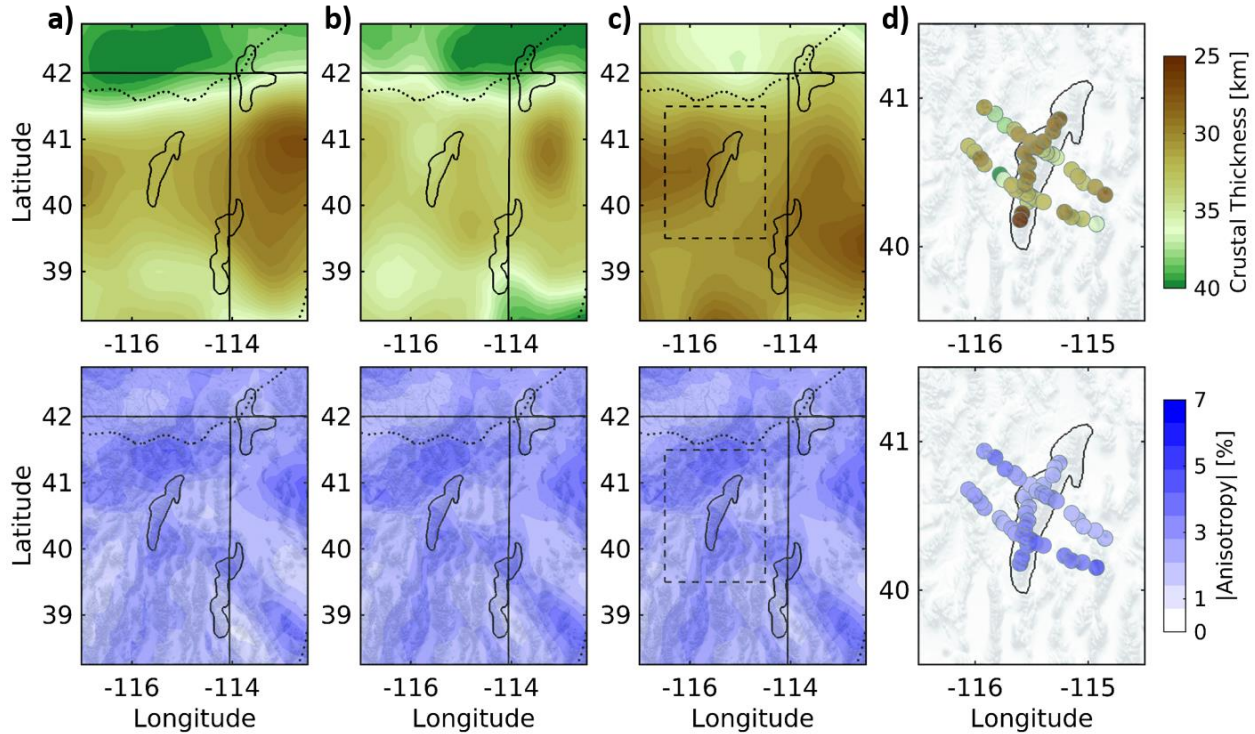
307 **Figure 3.** Prior model space range and b-spline parameterization of crustal V_S . (a) The range of V_S spanned by the
 308 prior distribution is shaded in the grey corridor. The example is shown with the regional mean Moho depth. (b)
 309 Parameterizations with 4 or 8 b-splines, which allow smoothly varying crustal V_S with a modest number of
 310 parameters compared to using discrete layers. In the different parameterization cases described in section 3.3 some,
 311 all, or none of the b-splines in the crust are allowed to be radially anisotropic.

312



313
 314 **Figure 4.** Data misfit maps for different inversion parameterizations. a-e) Chi-squared (χ^2) misfit maps for the five
 315 parameterization cases described in section 3.3. All maps correspond to inversions using the crustal thickness model
 316 of Schmandt et al., (2015). Regional mean χ^2 misfits are given in the upper left portion of each map. Maps in a-c
 317 correspond to inversions assuming isotropic V_s in the crust and exhibit high χ^2 misfits. Maps in d & e allow
 318 anisotropy in the entire crust and middle crust, respectively, and achieve similarly low regional mean χ^2 misfits.
 319

320 Each of the five inversion parameterization cases were run using three different regional
 321 crustal thickness models (Fig. 5; Schmandt et al., 2015; Buehler and Shearer, 2017; Shen and
 322 Ritzwoller, 2016), and an interpreted local crustal thickness model calculated below each station
 323 within the RMSE (Fig. 5; Litherland and Klemperer, 2017). The motivation for testing the
 324 different crustal thickness models is to determine if the strength and pattern of radial anisotropy
 325 are dependent on the choice of crust thickness model. Only subtle variations were found in the
 326 radially anisotropic structure as a result of different crustal thickness models (Fig. 5;
 327 Supplementary Information S4 and S5). So, we primarily present results using the crust thickness
 328 model of Schmandt et al., (2015) which contains measurements from both RMSE and TA data.



329
 330 **Figure 5.** Effects of crust thickness models on estimates of crustal radial anisotropy. a) The top panel shows the
 331 crust thickness model of Schmandt et al., (2015) and the bottom panel shows the depth-integrated absolute value of
 332 radial anisotropy from inversion cases 4 in which anisotropy is allowed in all 4 crustal b-splines. b,c) Similar to (a)
 333 but showing results using the crustal thickness models of Buehler and Shearer, (2017) and (c) Shen and Ritzwoller,
 334 (2016), respectively. (d) Similar to a-c except local crustal thickness results from Litherland and Klemperer, (2017)
 335 are only available beneath stations from the RMSE array. Dashed lines in (c) demarcate the area shown in (d).
 336 Distribution and magnitude of anisotropy are similar regardless of the choice of crust thickness model.
 337

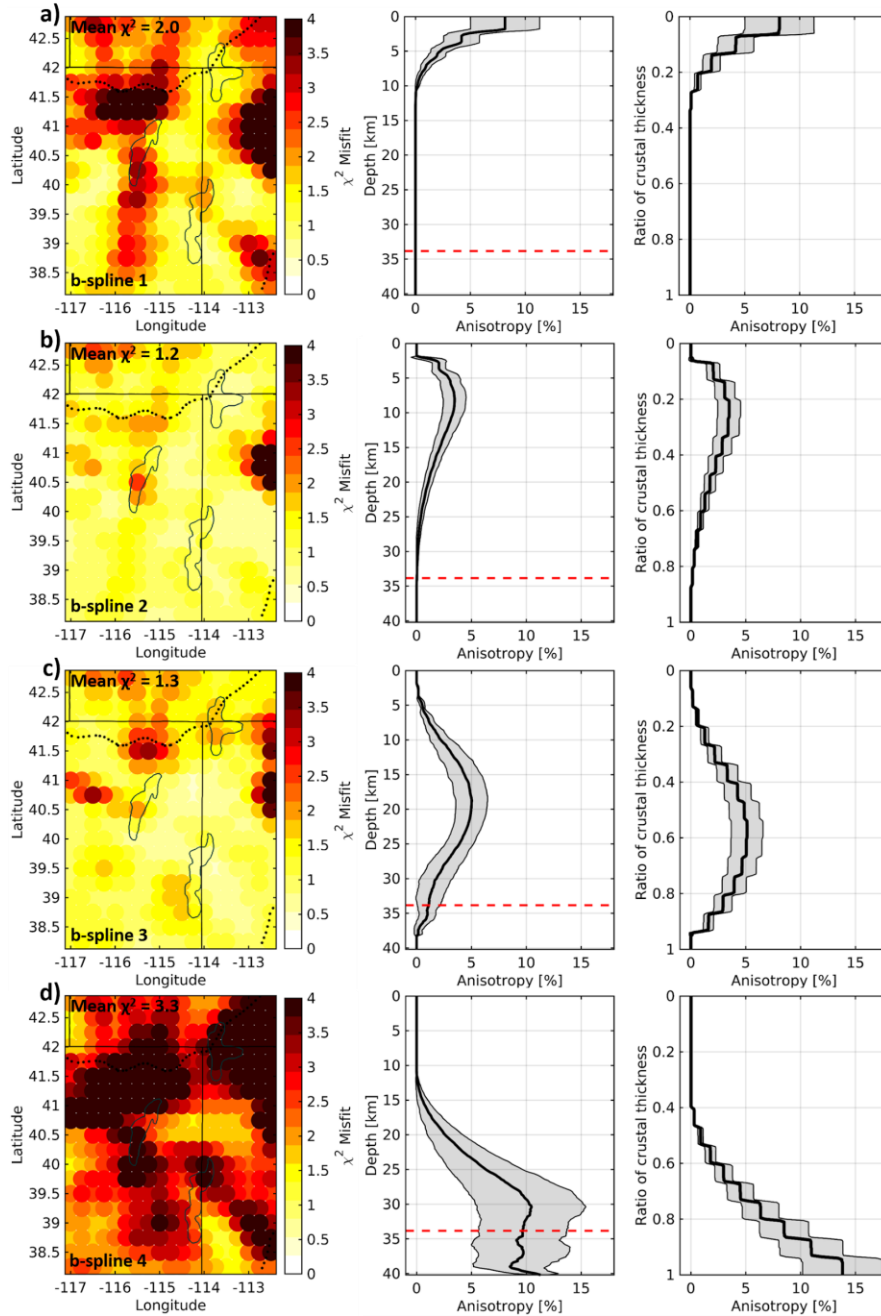
338 4. Results

339 4.1 Regional mean misfit and radial anisotropy

340 The five model parameterization cases provide insight into the importance of crustal radial
 341 anisotropy and its depth dependence. Assuming isotropy in the crust (cases 1-3) results in large
 342 regional mean χ^2 misfits of $\sim 4-7$ (Fig. 4). Compared to the fully isotropic crust and mantle in
 343 case 1, parametrization allowing upper mantle radial anisotropy (case 2), reduces the regional
 344 mean χ^2 misfit from 7.3 to 5.2. Case 3 explores whether doubling the isotropic parameters in the
 345 crust can explain the Rayleigh-Love discrepancy without introducing crustal anisotropy. This
 346 approach with 8 isotropic b-splines slightly reduces the regional mean χ^2 misfit from 5.2 to 4.1.
 347 Introduction of radial anisotropy throughout the crust (case 4) and anisotropy focused in the
 348 middle crust (case 5) result in superior regional mean χ^2 misfits of ~ 1 (Fig. 4; Supplementary
 349 Information S4). Persistently high mean χ^2 misfits located on the eastern edge of the study
 350 region are coincident with, and likely influenced by, the deep (~ 3 km in this location) Great Salt
 351 Lake basin structure (Mikulich and Smith, 1974).

352 To further evaluate the depth dependence of radial anisotropy, additional tests were
353 performed allowing the mantle and only a single crustal b-spline to be radially anisotropic in
354 each test. Individually introducing radial anisotropy for either b-spline 2 or 3 also achieves low
355 regional mean χ^2 misfits of 1.2 and 1.3, respectively (Fig. 6). Higher mean misfits of 2 and 3.3
356 were found when radial anisotropy was only allowed for b-spline 1 and 4, respectively. In these
357 cases of only allowing radial anisotropy for the uppermost or lowermost b-spline, larger peak
358 amplitudes of anisotropy were required, up to ~10-15%. Thus, crustal radial anisotropy is
359 necessary to adequately fit the Rayleigh and Love wave dispersion measurements and it is
360 possible to achieve similarly good fit to the data using only middle crustal radial anisotropy with
361 a peak magnitude of ~4-5%. Prior studies show that assuming uniform radial anisotropy through
362 the entire crust or confining it to the middle and lower crust, are alternative parameterization
363 approaches that can achieve regional mean χ^2 misfits of ~1 (e.g., Xie et al., 2015; Moschetti et
364 al., 2010a; Supplementary Information S6). These approaches are attractive for only requiring
365 one anisotropic parameter, however the tests conducted here demonstrate that just one
366 anisotropic parameter is equally effective if it is isolated to middle crustal depths (Fig. 6;
367 Supplementary Information S6).

368 The depth of the regional mean peak radial anisotropy varies from 8-20 km for the
369 parameterizations tested here that achieve regional mean χ^2 misfits of ~1. The shallowest peak
370 and smallest magnitude, 8 km & 3.5%, is found if only b-spline 2 is anisotropic. The deepest
371 peak depth and larger magnitude, 20 km & 5%, are found if only b-spline 3 is anisotropic.
372 Among parameterizations allowing multiple anisotropic b-splines the peak depth and magnitude
373 are 11 km & 5%, respectively, if all 4 b-splines are anisotropic (case 4) and 14 km & 3.5% if just
374 b-splines 2 & 3 are anisotropic (case 5). The larger peak magnitude that occurs when all 4 b-
375 splines are anisotropic is related to the introduction of negative anisotropy in much of the
376 regional the upper crust and more sporadically in the lower crust.



377
 378
 379
 380
 381
 382
 383
 384
 385
 386
 387
 388

Figure 6. Misfit maps and anisotropic depth profiles for tests with anisotropy in one isolated crustal b-spline. a) Left panel shows the regional mean χ^2 misfit map if anisotropy is only allowed for b-spline 1. The crustal b-spline that is allowed to be anisotropic is labeled in the lower left corner of the map and the regional mean χ^2 misfit is labeled in the upper left corner of the map. Middle panel shows the resulting radial anisotropy profile including the mean (black line) and 1 standard deviation corridor (grey) of the posterior distribution. Right panel also shows the radial anisotropy depth profile but with depth normalized to local crustal thickness. All results shown in this figure correspond to inversions assuming the regional crust thickness model of Schmandt et al., (2015). Regional mean χ^2 misfits are given in the upper left portion of each map. b-d) Similar to as but showing results for tests allowing anisotropy individually in b-splines 2-4, respectively. Note that individually allowing radial anisotropy for b-splines 2 and 3 fits the data better than for splines 1 and 4, while requiring smaller magnitudes of anisotropy.

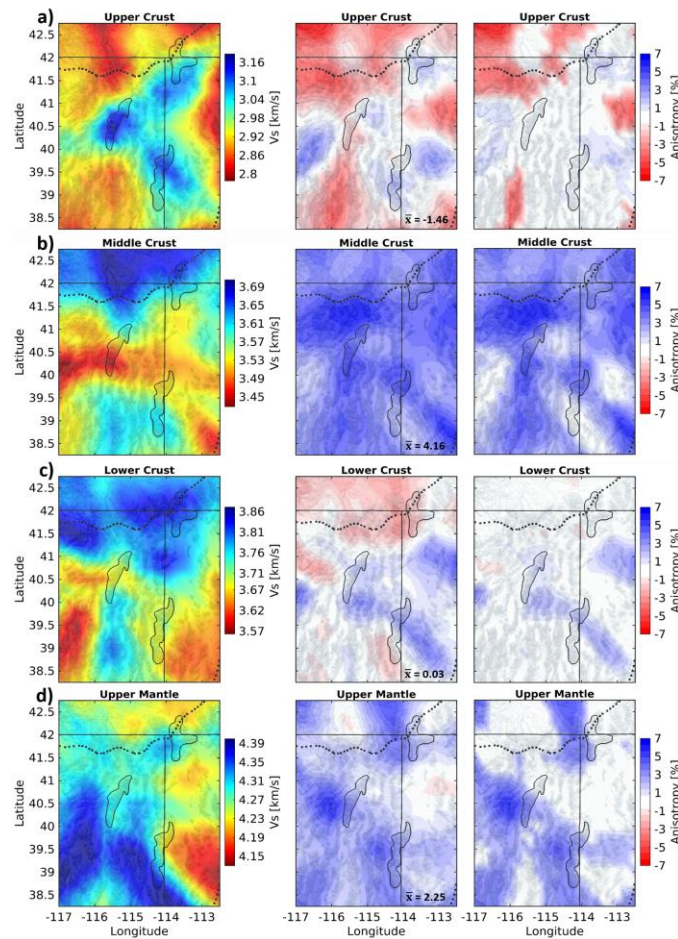
389 4.2 Variations in isotropic and anisotropic structure

390 Considering the broad depth sensitivity of surface waves we discuss the main results at 4
391 depth ranges: upper crust, middle crust, lower crust, and upper mantle (Fig. 7). The upper crust
392 is set to extend from 0 - 5 km, where the first b-spline depth range dominates and the shortest
393 period phase velocities in the inversion (6 s) have concentrated sensitivity. The depth extents of
394 the middle and lower crust are determined by evenly splitting the remaining crust thickness.
395 Since the major patterns in isotropic V_S variations remained consistent through the different
396 radial anisotropy parameterization cases (Supplementary Information S7), we focus on
397 describing inversion results from case 4 in which radial anisotropy was allowed at all crustal and
398 upper mantle depths. The plotted results represent the mean isotropic V_S and anisotropy of the
399 posterior distribution from the BMCC inversions for the region. To help identify where
400 anisotropy may not be necessary to provide a similarly good fit to the data we also provide plots
401 that show only areas where the absolute value of radial anisotropy has a statistical significance
402 greater than one standard deviation of the posterior distribution (Fig. 7, 8; Supplementary
403 Information S7 and S8-S10). In the upper crust negative radial anisotropy is more commonly
404 observed than positive radial anisotropy, and in many areas its significance exceeds one standard
405 deviation of the posterior distribution. The prevalence of upper crustal negative radial anisotropy
406 is consistent with some prior studies suggesting the presence of vertical to sub-vertical cracks at
407 low confining pressures (e.g., Crampin, 1994; Xie et al., 2013; Xie et al., 2017; Shirzad and
408 Shomali, 2014). The middle crust shows only positive radial anisotropy and its significance is
409 characteristically greater than one standard deviation of the posterior. In contrast, the lower crust
410 shows areas of negative anisotropy but the significance of these measurements is typically
411 smaller than one standard deviation of the posterior (Fig. 7).

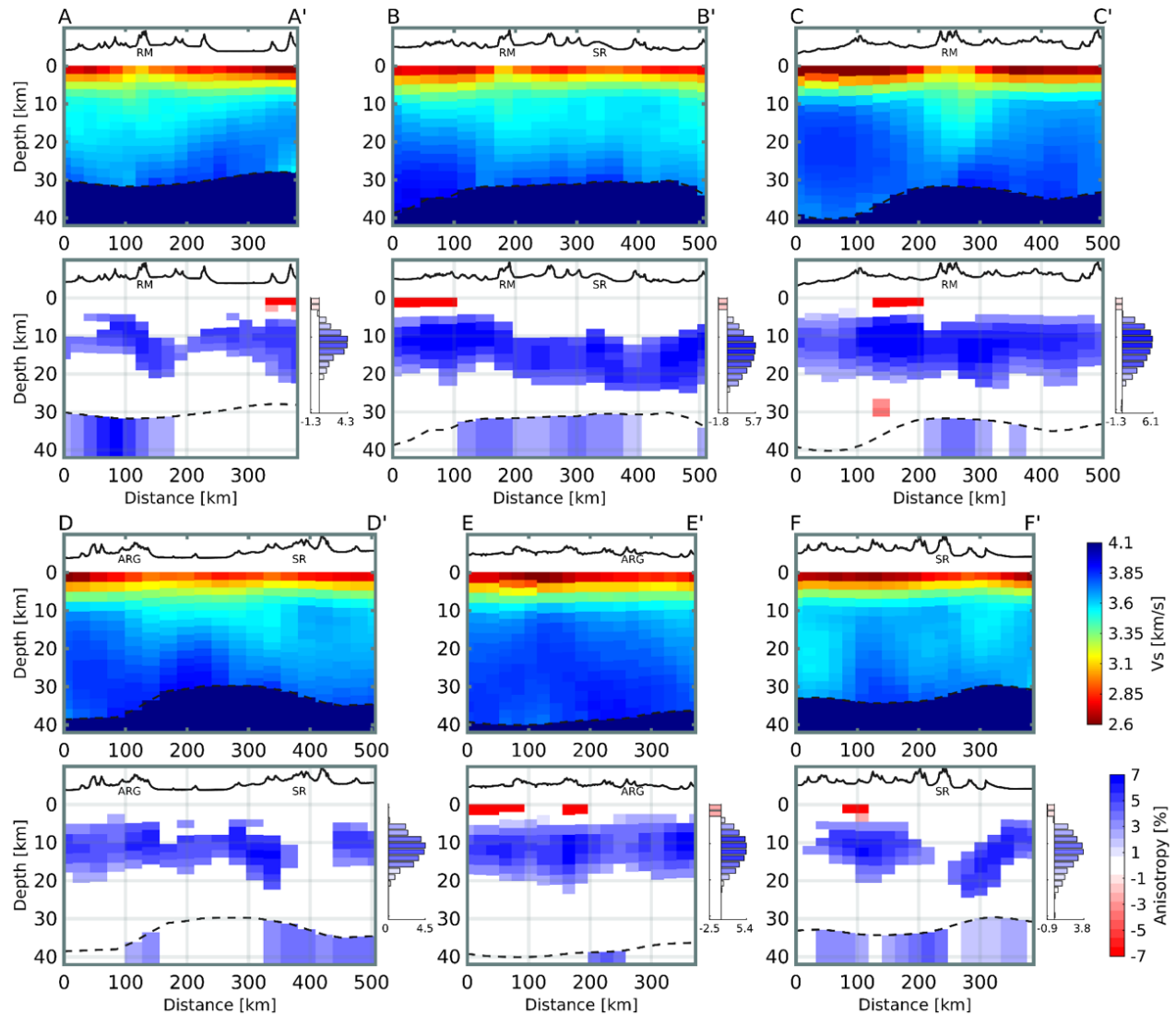
412 Distinctive V_S structure beneath the three MCC's is identified for isotropic V_S in the
413 upper crust, but the MCC's do not appear distinctive in radial anisotropy or middle-to-lower
414 crustal isotropic V_S (Fig. 7 & Fig. 8). At upper crustal depths the three MCC's exhibit isotropic
415 V_S that is ~5-7% higher than the regional mean (Fig. 7). In the middle crust the most prominent
416 isotropic V_S features are relatively high V_S (+3-5%) beneath the Snake River Plain and relatively
417 low V_S (-2 to -4%) in a ~west-east trending corridor that crosses the Ruby Mountains MCC but
418 extends across the study area (Fig. 7). In a North-South cross-section the low V_S in the middle
419 crust is co-located with the Ruby Mountains MCC (Fig. 8), but the map views show this is a
420 larger feature almost orthogonal to the strike of the Ruby Mountains (Fig. 7). In the lower crust,
421 the Snake River Plain is underlain by relatively high V_S (+4-6%) that extends southward across
422 the physiographic boundary with the Basin and Range (Fig. 7). At upper mantle depths the
423 highest V_S is found in the southwest portion of the study area toward the center of the Basin and
424 Range, and the lowest V_S is found near the northwestern edge of the Colorado Plateau (Fig. 7).
425 The patterns of isotropic V_S variations in the crust are consistent with prior tomography studies
426 using TA data (e.g., Moschetti et al., 2010a,b; Schmandt et al., 2015; Shen and Ritzwoller,
427 2016). Radial anisotropy cross-sections highlight the widespread positive radial anisotropy (+3-
428 5%) that forms a channel at middle crustal depths (Fig. 8). In general, the magnitude and depth

429 of radial anisotropy do not abruptly change near the MCC's. However, there is one notable local
 430 disruption of the middle crustal positive radial anisotropy channel near the Snake Range MCC
 431 (Fig. 8d,f).

432 Perhaps the most important new result from this study is the evidence suggesting depth-
 433 dependent radial anisotropy in the form of a regional middle-crustal channel of positive radial
 434 anisotropy (~3-5%). From a reductionist perspective it is informative that the parameterization
 435 tests show the Rayleigh-Love discrepancy can be adequately resolved by only introducing
 436 positive radial anisotropy in the middle crust (b-splines 2 and/or 3). Additionally, a peak
 437 magnitude of radial anisotropy of ~4% is sufficient if radial anisotropy is restricted to b-spline 2
 438 or depths of ~5-15 km, whereas greater magnitudes of up to 10-15% are needed to explain the
 439 Rayleigh-Love discrepancy if radial anisotropy is only allowed deeper or shallower (Fig. 6).



440 **Figure 7.** Depth averaged isotropic V_S and radial anisotropy maps for the upper crust, middle crust, lower crust, and
 441 upper mantle. (a) Depth averaged isotropic V_S and radial anisotropy of the upper crust. Left panel shows isotropic
 442 velocity. Middle panel shows radial anisotropy results. The depth averaged mean radial anisotropy of the map area (\bar{x})
 443 is given in the lower right corner. Right panel shows only results that have an absolute value of radial anisotropy
 444 with a statistical significance greater than one standard deviation of the posterior distribution. The upper crust maps
 445 average results between 0 and 5 km while the extent of depth averaging of the middle and lower crust is determined
 446 by evenly splitting the remaining thickness between 5 km and the Moho at each inversion point. (b-d) Same as (a)
 447 but for the middle and lower crust and upper mantle, respectively. All results shown in this figure are from inversion
 448 case 4 and correspond to inversions assuming the regional crust thickness model of Schmandt et al., (2015).
 449

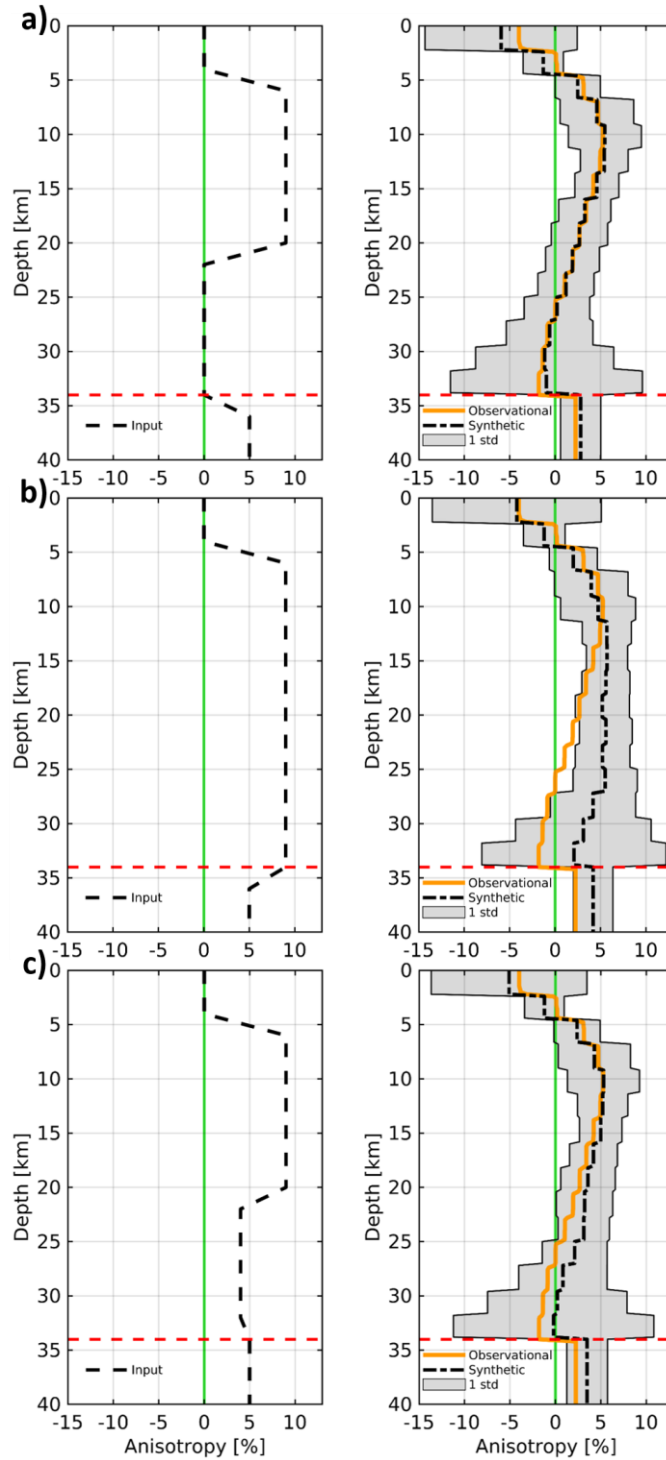


450
 451 **Figure 8.** Cross sections (see figure 1) showing isotropic V_s and anisotropy results from inversion case 4 using the
 452 crustal thickness (dashed line) model of Schmandt et al., (2015). Bar charts right of anisotropy cross sections show
 453 average anisotropy profiles with depth for each cross section. Anisotropy minima and maxima are labeled on the x
 454 axis of each profile and colors correspond to anisotropy color bar. The radial anisotropy cross-sections (lower
 455 panels) in a-f show only results that have an absolute value of radial anisotropy with a statistical significance greater
 456 than one standard deviation of the posterior distribution. Topography is exaggerated 3 times in the profiles at the top
 457 of each panel.

458
 459
 460
 461
 462
 463

464 **4.3 Synthetic resolution tests**

465 Resolution tests using synthetic dispersion curves generated from known V_s models confirm that
466 a middle crustal channel of radial anisotropy is resolvable and provide insight into the optimal
467 depth range and magnitude of anisotropy for matching the observational results. The synthetic V_s
468 model posterior that best matches the regional mean structures includes 9% radial anisotropy
469 from 6-22 km depth and 5% radial anisotropy in the upper mantle (Fig. 9a). A test with 9% radial
470 anisotropy extending from 6 km to the Moho does not match the diminishing radial anisotropy
471 with depth found in the inversion results based on observational data (Fig. 9b). A test with
472 weaker lower crustal radial anisotropy of 4% is also consistent with the regional mean from the
473 observational results (Fig. 9c). Therefore, although the magnitude of anisotropy in the lower
474 crust is not as strong as it is in the middle crust, the dispersion data cannot discriminate whether
475 lower crustal radial anisotropy is somewhat weaker than that of the middle crust or absent
476 entirely.



477
 478 **Figure 9.** Synthetic resolution tests. (a) Left panel shows resolution test input (dashed line) of 9% radial anisotropy
 479 from 6-22 km and 5% in the upper mantle. Right panel shows resulting mean radial anisotropy model (dash-dotted
 480 line) from the forward calculation and one sigma corridor (shaded gray region) of the modeled posterior distribution.
 481 Dark green line shows observed mean model from inversion case 4. (b) Same as (a) but with 9% radial anisotropy
 482 throughout the crust as input. (c) Same as (b) but with 4% radial anisotropy in the lower crust, 22 km to 34 km.
 483

484 **4.4 Uncertainties due to modeling assumptions**

485 Perhaps the most important source of uncertainty in the results lies in the validity of the radial
486 anisotropy assumption. In this study, transverse isotropy (referred to as hexagonal symmetry in
487 crystallography) with a vertical symmetry axis is assumed. This assumption is approximately
488 valid for many deformed crustal rock samples (Erdman et al., 2013; Brownlee et al., 2017) and is
489 common in studies seeking to explore seismic anisotropy via the Rayleigh-Love discrepancy. In
490 some studies, this is also referred to as ‘apparent radial anisotropy’ (e.g., Xie et al., 2015; Xie et
491 al., 2017, Feng et al., 2019). However, different forms of anisotropy and spatial variations in the
492 tilt of the symmetry axis are likely to be present based on common crustal lithologies (Tatham et
493 al., 2008; Ward et al., 2012; Erdman et al., 2013; Brownlee et al., 2017; Almqvist and Mainprice,
494 2017). Allowing for more complex forms of anisotropy, such as an oriented hexagonal or
495 orthorhombic tensor would come with the tradeoff of estimating a greater number of model
496 parameters, and prior results find that our study area is relatively well-suited to the simpler
497 assumption of transverse isotropy. Xie et al., (2015) inverted surface wave dispersion and
498 ellipticity measurements allowing for hexagonal anisotropy with a spatially variable tilt axis, and
499 found that dip angles of the symmetry axis are relatively small, $\sim 15\text{-}25^\circ$, in the northeastern
500 Basin and range compared to the western U.S. average, $\sim 25\text{-}30^\circ$. This would cause our estimates
501 of radial anisotropy to be slight underestimates compared to the oriented elastic tensor approach
502 of Xie et al., (2015). The simpler approach adopted here allows for efficient testing of several
503 parameterizations that provide new insights into the depth dependence of radial anisotropy.

504 Another source of modeling uncertainty is the assumption of an empirical V_P/V_S scaling
505 (Brocher, 2005), which could bias the radial anisotropy results especially in cases of strongly
506 anomalous V_P/V_S that might be associated with deep sedimentary basins or the alpha-beta quartz
507 transition in thick continental crust (Gao and Lekić, 2018). In the absence of strong constraints
508 on V_P across the study area we consider the empirical V_P/V_S scaling relationship a reasonable
509 assumption. Future studies incorporating additional measurements such as Rayleigh wave
510 ellipticity (e.g., Lin et al., 2014; Gao and Lekić, 2018) and P wave reflectivity from ambient
511 noise or coda autocorrelation (e.g., Gorbatov et al., 2012; Tibuleac and von Seggern, 2012;
512 Delph et al., 2019) offer opportunities to better mitigate tradeoffs between V_P/V_S and crustal
513 radial anisotropy.

514 **5. Discussion**

515 **5.1 Upper Mantle**

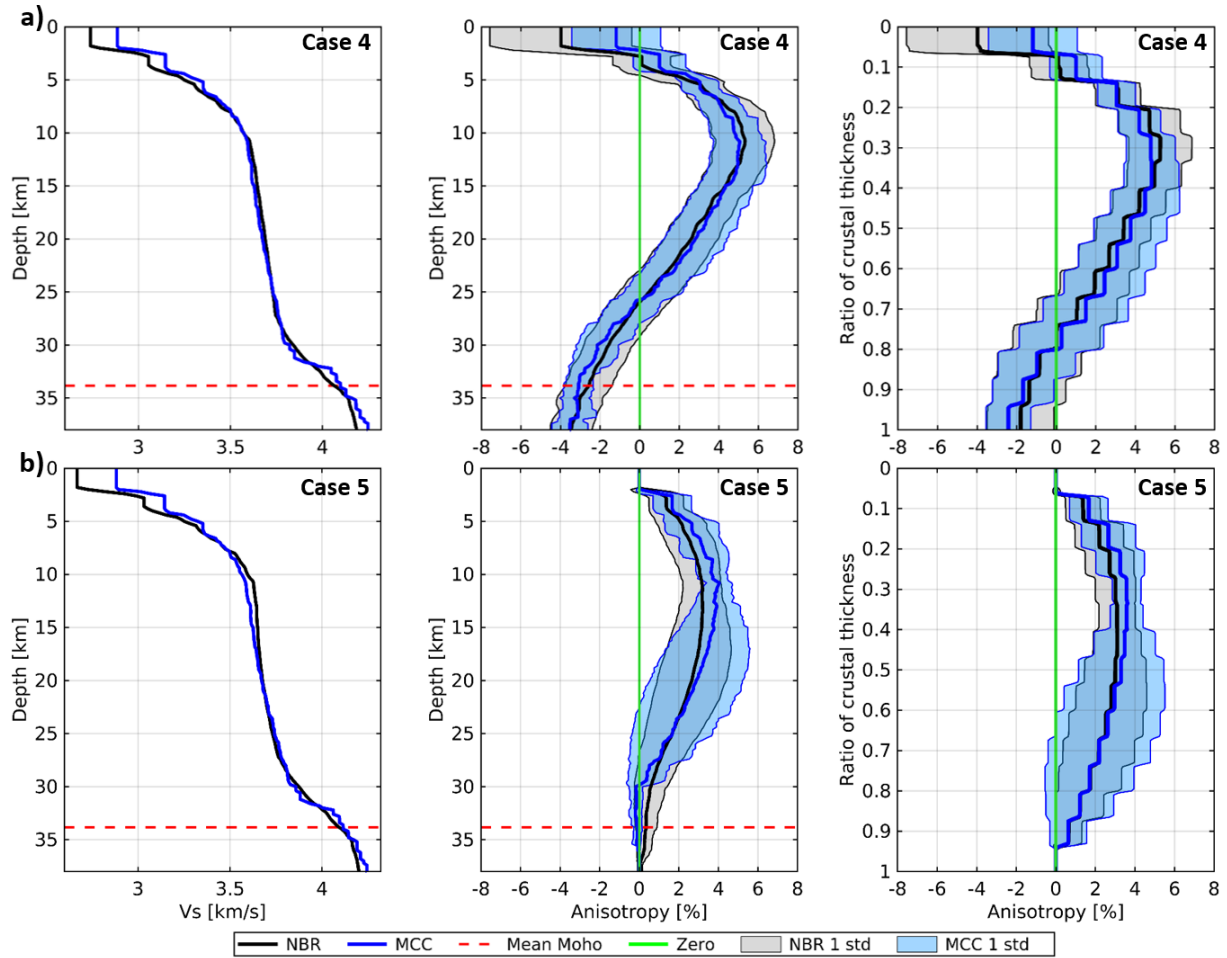
516 The surface wave period range used here (5-30s) is most sensitive to crustal structure, but due to
517 tradeoffs between lower crust and upper mantle structure it is worth noting that the isotropic and
518 anisotropic upper mantle results from this study are consistent with previous studies
519 incorporating longer period measurements. Relatively high isotropic V_S , $\sim 4.3\text{-}4.4$ km/s, in the
520 uppermost mantle of the southwest portion of the study region agrees with prior V_S tomography
521 incorporating longer period surface waves and receiver functions (Shen and Ritzwoller, 2016)

522 and appears to be correlated with positive radial anisotropy in the same region (Fig. 7). The
523 results presented here also confirm that positive radial anisotropy of ~2-5% is widespread in the
524 uppermost mantle beneath the Basin and Range as found by recent long period waveform
525 tomography (Yuan et al., 2014; Zhu et al., 2017; Clouzet et al., 2018).

526 **5.2 Links between MCC's and V_S structure**

527 The anomalous degree of exhumation and extension evident at the surface in MCC's motivates
528 inquiry into how MCC formation is manifested in sub-surface V_S structure. The three MCC's in
529 the study area are closely correlated with relatively high V_S , + 4-7%, in the upper crust (Fig. 7).
530 Continental crustal V_S generally increases with depth (Christiansen and Mooney, 1995; Laske et
531 al., 2013; Tesauro et al., 2014; Shen et al., 2016) and in these locations crustal rocks have been
532 exhumed from the middle-to-lower crust to the surface. We therefore interpret these relatively
533 high V_S regions to be a simple consequence of the locally anomalous exhumation (Fig. 7a).
534 Comparison of the average V_S structure beneath the three MCC's with the average across the
535 study area further shows the distinctly higher V_S in the upper crust (Fig. 10). In contrast, middle-
536 to-lower crustal V_S and radial anisotropy depth profiles averaged beneath the three MCC's are
537 strikingly similar to those averaged across the study area (Fig. 10). This similarity suggests that
538 either MCC formation had little effect on deep crustal structure (V_S and anisotropy) or that the
539 effect of MCC formation on deep crustal structure has been overprinted.

540 Models of MCC formation, particularly for rapidly exhumed MCC's, predict locally sub-
541 vertical flow lines associated with anomalous levels of exhumation and partial melting of the
542 middle crust (Rey et al., 2009a,b). In the majority of the region surrounding MCC's sub-
543 horizontal strain in the ductile crust is expected to dominate and supply the crustal mass
544 necessary to balance rapid exhumation (Tirel et al., 2008; Wu et al., 2015, 2016). Sub-vertical
545 strain organization in a transverse isotropy (or hexagonal symmetry) paradigm would likely
546 produce a negative radial anisotropy signal locally beneath the MCC's, or at least diminish the
547 regionally prevalent positive radial anisotropy due to spatial averaging of complex structural
548 transitions (e.g., Okaya et al., 2018). However, we generally do not find distinctly weaker or
549 negative radial anisotropy beneath the three MCC's. Instead, they generally exhibit positive
550 radial anisotropy in the middle crust and weaker radial anisotropy in the lower crust, similar to
551 the surrounding region. The 70-km spacing of the TA may limit detection of local V_S variations
552 in the middle-to-lower crust beneath the Snake Range and ARG, but the dense ~5-10 km spacing
553 of the RMSE array is capable of resolving distinctive local V_S structure if it exists beneath the
554 Ruby Mountains. Additionally, we note that the available seismic sampling is sufficient to detect
555 locally higher upper crustal isotropic V_S associated with all three MCC's. To explain the absence
556 of distinctive structure (V_S and anisotropy) in the middle-to-lower crust, we suggest that ductile
557 deformation promoted by a hot geotherm during and after middle Miocene regional scale
558 extension of the Basin and Range effectively homogenized deep crustal V_S structure near the
559 MCC's.



560
561
562
563
564
565
566
567
568
569
570
571
572
573
574
575
576
577
578
579

Figure 10. Comparison of V_S structure beneath MCC's and the surrounding region. (a) Left panel shows mean isotropic V_S profiles of the regional northern Basin and Range (black lines) and subset MCC's (blue lines). Notice high V_S in the upper crust of the MCC profile relative to the northern Basin and Range. Center panel shows mean crustal radial anisotropy depth profiles of the regional northern Basin and Range (black lines) and subset MCC's (blue lines) from inversion cases 4. Shaded gray and blue regions are 1 sigma corridors of the northern Basin and Range and subset MCC's, respectively. Notice similarity in magnitude and distribution between the northern Basin and Range and MCC profiles. There are relatively few profiles that extend to depths greater than 35 km and therefore the number of measurements included in the mean profile decreases with increasing depth. In the absence of depth averaging the $\sim 5\%$ peak magnitude of anisotropy observed here surpasses the depth averaged middle crust mean radial anisotropy of the map area, $\bar{x} = 4.16\%$, as reported in Fig 7b. Right panel is same as center panel but normalized to crustal thickness. Notice largely isotropic behavior of lower crust relative to the middle crust. (b) Same as (a) but for inversion case 5. Anisotropy peaks in the middle crust in inversion cases 4 and 5 demonstrating similarity in the depth distribution of anisotropy.

580 **5.3 Concentration of anisotropy in a middle crustal channel**

581 Prior studies established the presence of positive radial anisotropy in the Basin and Range crust
582 (Moschetti et al., 2010a; Xie et al., 2015). One of the main goals of this study is to evaluate
583 potential depth dependence of radial anisotropy to provide insight regarding the deformation
584 regimes and compositions that are most likely to contribute to the development of large-scale
585 crustal radial anisotropy. The results from several different inversion parameterization tests
586 provide evidence that the Rayleigh-Love discrepancy in the northeastern Basin and Range is
587 most simply addressed by a channel of positive radial anisotropy in the middle crust from ~6-22
588 km depth (Fig. 9 & 10). By simplicity we mean that radial anisotropy is only required in a subset
589 of the crust and that a relatively small magnitude of anisotropy is sufficient to simultaneously fit
590 the Rayleigh and Love wave dispersion data (Fig. 4 & 5).

591 Below we consider potential reasons why radial anisotropy may be focused at middle
592 crustal depths by discussing the potential roles of depth-dependent crustal composition and
593 rheology. Mineral composition is a key consideration because it controls the potential magnitude
594 of CPO development and predicts how a particular strain orientation would manifest itself in
595 measurements of seismic radial anisotropy (e.g., Ward et al., 2012; Erdman et al., 2013). A
596 conventional perspective is that the middle crust has an intermediate bulk composition largely
597 containing amphibolite facies rocks and the lower crust has a mafic-to-intermediate bulk
598 composition largely containing granulite facies rocks (Rudnick and Fountain, 1995). However,
599 the prevalence of relatively mafic lower continental crust remains a subject of debate (Hacker et
600 al., 2015). Rheology is expected to vary with depth from an elastic upper crust that hosts
601 frictional fault-controlled deformation to a time-dependent ductile middle-to-lower crust that
602 hosts flow within shear zones or distributed throughout larger volumes (e.g., Kohlstedt et al.,
603 1995; Bürgmann and Dresen, 2008; Thatcher and Pollitz, 2008). Composition and rheology are
604 used here as a framework for discussion but they are not independent. They are strongly linked
605 by depth-dependent temperature and pressure conditions that change the relevant constitutive
606 relationships and determine the stability of specific minerals.

607 From a compositional perspective, studies of seismic anisotropy in the continental crust
608 often highlight the potential importance of CPO in mica-rich foliated metamorphic rocks because
609 they are abundant and single crystal mica is one of the most anisotropic crustal minerals (Weiss
610 et al., 1999; Lloyd et al., 2009). Hexagonal symmetry (or transverse isotropy) is a valid
611 assumption for single crystal mica and it remains an effective approximation for many bulk rock
612 samples with abundant mica (e.g., Nishizawa and Yoshino, 2001; Lloyd et al., 2009; Bostock
613 and Christensen, 2012; Erdman et al., 2013; Brownlee et al., 2017). Amphibole is another
614 common crustal mineral with potential to contribute to spatially-averaged crustal seismic
615 anisotropy (Tatham et al., 2008; Brownlee et al., 2017). However, single crystal amphiboles are
616 much less anisotropic than micas, and amphibole-rich rocks commonly exhibit a component of
617 orthorhombic symmetry (Brownlee et al., 2017) which would not be accurately represented with
618 radial anisotropy. Quartz, in aggregate, is not likely to develop strong CPO in high strain
619 environments (Rahl and Skemer, 2016) but it can destructively interfere with bulk anisotropy in

620 lithologies with mica or amphibole (Ward et al., 2012). Mica-bearing metamorphic rocks are
621 generally abundant in the middle crust and rock samples exhumed from the Ruby Mountains
622 MCC exhibit ~4-19% V_S anisotropy that is positively correlated with mica content (Erdman et
623 al., 2013).

624 We suggest that mica-bearing metamorphic rocks with a sub-horizontal foliation (sub-
625 vertical slow-axis symmetry) are a viable explanation for the observed middle crustal positive
626 radial anisotropy signal. Geodynamic models of regional-scale extension including core complex
627 development (Wu et al., 2015, 2016; Tirel et al., 2008) and seismic reflection imaging support
628 the prevalence of sub-horizontal fabrics in the middle crust due to low-angle detachment faults
629 and shear zones (Klemperer et al., 1986; McCarthy, 1986; Hauser et al., 1987; Holbrook et al.,
630 1991; Valasek et al., 1989; Stoerzel and Smithson, 1998). Weaker radial anisotropy in the lower
631 crust is consistent with the interpretation that mica-bearing metamorphic rocks are a major
632 contributor to the middle crustal channel of positive radial anisotropy. This is because higher
633 temperatures (>600-700° C) approaching the Moho would lead to diminished abundance of
634 hydrous phases like micas in granulite facies lower crust (e.g., Mahan, 2006).

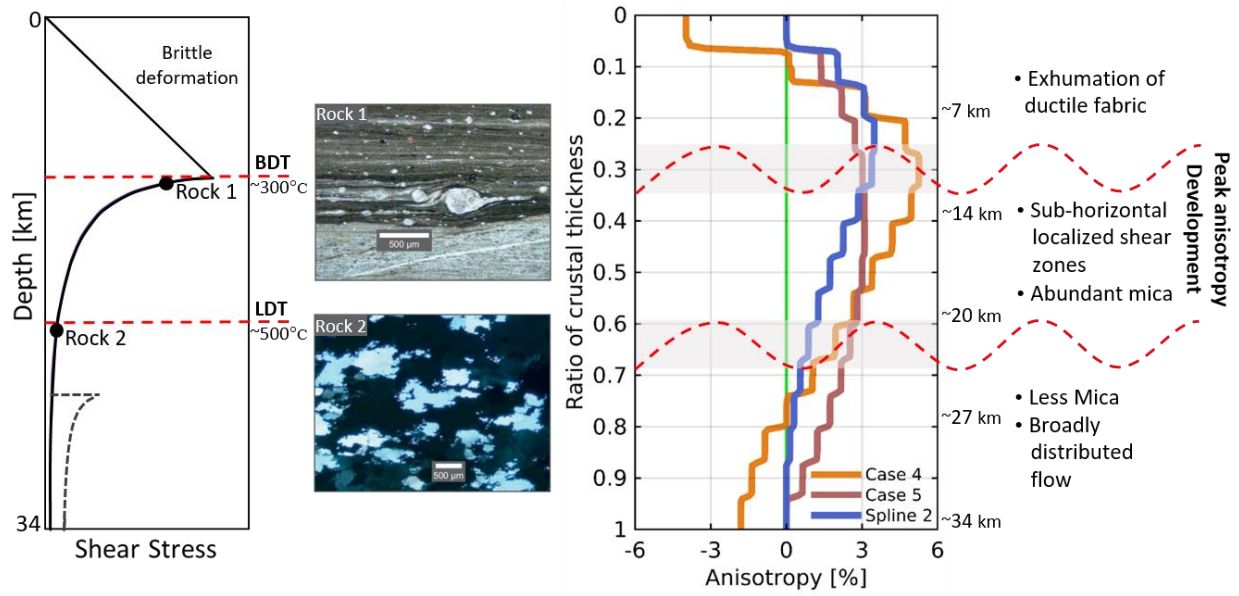
635 Rheological variations with depth may also contribute to the depth-dependent radial
636 anisotropy in the study area. At geological time scales ductile flow is expected in the middle and
637 lower crust of the Miocene-to-present Basin and Range (e.g., Thatcher and Pollitz, 2008; Tirel et
638 al., 2008). However, decreasing shear stress and effective viscosity with depth, and increasing
639 temperature with depth, could alter the potential for generation of large-scale seismic anisotropy.
640 Onset of dislocation creep at lower stress conditions in the hotter lower crust favors larger
641 dynamically recrystallized grain sizes and more distributed deformation, whereas onset of creep
642 at higher stress conditions in the middle crust favors grain size reduction that leads to weakening
643 and strain localization (Stipp and Tullis, 2003; Behr and Platt, 2011; Cooper et al., 2017). To
644 first order, textures, fabrics and compositions of middle and lower crustal rocks obtained from
645 Basin and Range MCC's reflect this transition (Fig. 11; Cooper et al., 2017). Cooper et al.,
646 (2017) identified two major rheological boundaries in Basin and Range MCC's, the brittle-
647 ductile transition (BDT) and a deeper temperature-dependent boundary referred to as the
648 localized-distributed transition (LDT). In this context, we suggest that positive radial anisotropy
649 may be more effectively generated in localized shear zones closer to the top of the ductile
650 deformation region in the middle crust. A regional median heat flux of 79 mWm^{-2} (Hasterok and
651 Chapman, 2007) and thermal conductivity between $2.2\text{-}3.3 \text{ Wm}^{-1}\text{K}^{-1}$ (Whittington et al., 2009)
652 corresponds to a geothermal gradient range of $\sim 25\text{-}35^\circ\text{C/km}$. Taking the $\sim 300^\circ\text{C}$ isotherm as a
653 proxy (e.g., Cooper et al., 2017) we estimate a modern BDT depth range of $\sim 9\text{-}12 \text{ km}$ (Fig. 11).
654 Results indicating that the mid crustal channel of anisotropy extends above the estimated BDT,
655 $\sim 6 \text{ km}$ depth, suggests preservation of anisotropy in rocks that were deformed below the BDT
656 and have subsequently been exhumed. Decaying strength of anisotropy in the lower crust may
657 reflect the gradual LDT below which deformation is distributed across larger volumes and
658 recrystallization is more rapid. The $\sim 500^\circ \text{C}$ temperature of the inferred LDT in the Basin and
659 Range is somewhat cooler than the petrologic transition to relatively mica-poor granulite facies,

660 ~600-700° C. The similar depths of such boundaries would not likely be resolvable with
661 dispersion data alone. Therefore, it is not feasible, based on depth alone, to determine if the
662 rheological or compositional transition has a more important influence on radial anisotropy.

663 The history of magmatism in the Basin and Range is another important factor in
664 evaluating the potential compositional and rheological origins of depth-dependent radial
665 anisotropy. Substantial influx of mafic melt into the lower crust is expected during the
666 voluminous Eocene-Miocene ignimbrite flare-up (e.g., Gans, 1987; Best and Christiansen, 1991).
667 This event likely had long lasting consequences on crustal composition and rheology. Following
668 flat-slab subduction during the Laramide orogeny the regional lithosphere was likely cooler and
669 contained more abundant hydrous minerals (Humphreys et al., 2003), but subsequent heating and
670 flux of melt through the lithosphere would have dehydrated the lower crust and promoted a more
671 mafic bulk composition (Gans, 1987). A dry lower crust in the contemporary Basin and Range is
672 consistent with a scenario in which decreasing mica content in the lower crust leads to
673 decreasing radial anisotropy.

674 Mafic intrusions would have competing effects on lower crustal rheology through
675 thermal weakening that decays with time superimposed on long-term addition of primitive basalt
676 or cumulate compositions that are more viscous than typical intermediate composition crust (e.g.,
677 Schutt et al., 2018). Seismic reflectivity of the Basin and Range crust peaks in the middle crust
678 but weaker sub-horizontal reflectors are still common in the lower crust and are frequently
679 attributed to mafic intrusions (Holbrook et al., 1991; Klemperer et al., 1986; McCarthy, 1986). A
680 more mafic lower crust following Miocene opening of the Basin and Range would complicate
681 the possibility of a regionally extensive LDT. Expanding on this idea, the deeply exhumed rocks
682 that Cooper et al., (2017) used to define the LDT may preferentially represent zones of weakness
683 during MCC formation rather than modern regionally-averaged rheology. Sill-like intrusions are
684 interpreted to contribute to strong positive radial anisotropy in active magmatic systems as a
685 result of shape-preferred orientation (SPO) due to large V_S contrasts between partially molten
686 and sub-solidus crustal rocks (Jaxybulatov et al., 2014; Harmon and Rychert, 2015; Jiang et al.,
687 2018; Lynner et al., 2018). However, crystallized basaltic sills embedded in an intermediate to
688 mafic lower crust may not have large enough velocity contrasts for SPO to cause detectable
689 radial anisotropy (Schmandt et al., 2019). For example, strong positive radial anisotropy, ~12%,
690 is found beneath Yellowstone caldera but older calderas beneath the Snake River Plain are
691 underlain by relatively isotropic crust (Jiang et al., 2018).

692
693
694
695
696
697



698
 699 **Figure 11.** Synthesis of results. Left panel shows typical crustal strength profile and approximate depth ranges at
 700 which the brittle to ductile transition (BDT) and localized distributed transition (LDT) occur (dashed red line) in the
 701 Basin and Range. Possible mafic addition to the lower crust is represented with a step in the lower crust (black
 702 dashed line). Approximate temperatures of the BDT and LDT are labeled and are adopted from Cooper et al.,
 703 (2017). Center shows microphotographs (originally from Platt et al., (2015) but also used in Cooper et al., (2017)) of
 704 representative middle (Rock 1) and lower (Rock 2) crustal rocks exhumed from the RMCC. Depth and stress
 705 environments from which the rocks were exhumed are labeled on crustal strength profile. As temperature increases
 706 and viscosity decreases with depth mica is lost, grains grow larger and distributed deformation diminishes
 707 anisotropy producing layering fabrics. Right panel shows study are mean anisotropy distribution with depth
 708 normalized to crustal thickness for inversion cases 4 and 5, and the inversion that allows only b-spline 2 to be
 709 anisotropic. Approximate depth ranges are labeled every 0.2 ratio of crustal thickness. Approximate depth ranges of
 710 peak anisotropy development, preservation after exhumation, and loss with increasing depth as discussed in the text
 711 are labeled to the right of center panel.
 712

713 6. Conclusion

714 Rayleigh and Love wave dispersion measurements were inverted for radially anisotropic V_S
 715 structure of the crust and uppermost mantle beneath an area of the northeastern Basin and Range
 716 including three MCC's. Tests of several parameterizations provided new evidence that positive
 717 radial anisotropy is strongest at depths of ~8-20 km across the region. The three MCC's have
 718 distinctive high isotropic V_S in the upper crust, but they do not interrupt the regional channel of
 719 radial anisotropy focused in the middle crust. Sub-horizontal foliation (sub-vertical slow axis
 720 symmetry) of mica-bearing lithologies in ductile shear zones and detachments is a viable origin
 721 for the positive radial anisotropy focused in the middle crust. The decay of radial anisotropy with
 722 depth in the lower crust could result from decreased mica abundance as high temperatures and
 723 influx of mantle melts since the Oligocene favor a dry and increasingly mafic mean composition.
 724 Rheological transition to more broadly distributed viscous deformation at lower crustal high
 725 temperatures may also contribute to diminishing anisotropy with depth. The absence of
 726 distinctive radial anisotropy beneath the three MCC's suggests that anisotropy generated during
 727 peak metamorphism, which generally occurred in the Oligocene, was subsequently overprinted

728 by regionally pervasive extensional deformation of the ductile crust during and after the middle
729 Miocene. The results motivate further investigation of the depth dependence of crustal
730 anisotropy in other areas of continental deformation to gain a global perspective on the relative
731 importance among potential compositional and rheological contributions to crustal anisotropy.
732

733 **Acknowledgements**

734 The facilities of the Incorporated Research Institutions for Seismology (IRIS) Data Services, and
735 specifically the IRIS Data Management Center (<https://ds.iris.edu/ds/nodes/dmc/>), were used for
736 access to waveforms, related metadata, and/or derived products from seismograph networks
737 (listed in supplemental material) used in this study. IRIS Data Services are funded through the
738 Seismological Facilities for the Advancement of Geoscience and EarthScope Proposal of the
739 National Science Foundation (NSF) under Cooperative Agreement EAR-1261681. S. Klemperer
740 led the collection of the RMSE data and engaged in helpful discussions. J. Selverstone and W.
741 Behr provided valuable feedback during the project. This research was supported by NSF EAR-
742 1554908.

743

744 **References**

- 745 Almqvist, B. S., & Mainprice, D. (2017). Seismic properties and anisotropy of the continental
746 crust: predictions based on mineral texture and rock microstructure. *Reviews of*
747 *Geophysics*, 55(2), 367-433.
- 748 Babuska, V., & Cara, M. (1991). *Seismic anisotropy in the Earth* (Vol. 10). Springer Science &
749 Business Media.
- 750 Backus, G. E. (1962). Long-wave elastic anisotropy produced by horizontal layering. *Journal of*
751 *Geophysical Research*, 67(11), 4427-4440.
- 752 Barnes, C. G., Burton, B. R., Burling, T. C., Wright, J. E., & Karlsson, H. R. (2001). Petrology
753 and geochemistry of the late Eocene Harrison Pass pluton, Ruby Mountains core
754 complex, northeastern Nevada. *Journal of Petrology*, 42(5), 901-929.
- 755 Bennett, R. A., Wernicke, B. P., Niemi, N. A., Friedrich, A. M., & Davis, J. L. (2003).
756 Contemporary strain rates in the northern Basin and Range province from GPS data.
757 *Tectonics*, 22(2).
- 758 Bensen, G. D., Ritzwoller, M. H., Barmin, M. P., Levshin, A. L., Lin, F., Moschetti, M. P.,
759 Shapiro, N.M., & Yang, Y. (2007). Processing seismic ambient noise data to obtain
760 reliable broad-band surface wave dispersion measurements. *Geophysical Journal*
761 *International*, 169(3), 1239-1260.
- 762 Best, M. G., & Christiansen, E. H. (1991). Limited extension during peak Tertiary volcanism,
763 Great Basin of Nevada and Utah. *Journal of Geophysical Research: Solid Earth*, 96(B8),
764 13509-13528.
- 765 Behr, W. M., & Platt, J. P. (2011). A naturally constrained stress profile through the middle crust
766 in an extensional terrane. *Earth and Planetary Science Letters*, 303(3-4), 181-192.

767 Brocher, T. M. (2005). Empirical relations between elastic wavespeeds and density in the Earth's
768 crust. *Bulletin of the seismological Society of America*, 95(6), 2081-2092.

769 Buehler, J. S., & Shearer, P. M. (2017). Uppermost mantle seismic velocity structure beneath
770 USArray. *Journal of Geophysical Research: Solid Earth*, 122(1), 436-448.

771 Block, L., & Royden, L. H. (1990). Core complex geometries and regional scale flow in the
772 lower crust. *Tectonics*, 9(4), 557-567.

773 Bostock, M. G., & Christensen, N. I. (2012). Split from slip and schist: Crustal anisotropy
774 beneath northern Cascadia from non-volcanic tremor. *Journal of Geophysical Research:*
775 *Solid Earth*, 117(B8).

776 Brownlee, S. J., Schulte-Pelkum, V., Raju, A., Mahan, K., Condit, C., & Orlandini, O. F. (2017).
777 Characteristics of deep crustal seismic anisotropy from a compilation of rock elasticity
778 tensors and their expression in receiver functions. *Tectonics*, 36(9), 1835-1857.

779 Bürgmann, R., & Dresen, G. (2008). Rheology of the lower crust and upper mantle: Evidence
780 from rock mechanics, geodesy, and field observations. *Annu. Rev. Earth Planet. Sci.*, 36,
781 531-567.

782 Camp, V. E., Pierce, K. L., & Morgan, L. A. (2015). Yellowstone plume trigger for Basin and
783 Range extension, and coeval emplacement of the Nevada–Columbia Basin magmatic
784 belt. *Geosphere*, 11(2), 203-225.

785 Cheng, C., Chen, L., Yao, H., Jiang, M., & Wang, B. (2013). Distinct variations of crustal shear
786 wave velocity structure and radial anisotropy beneath the North China Craton and
787 tectonic implications. *Gondwana Research*, 23(1), 25-38.

788 Christensen, N. I., & Mooney, W. D. (1995). Seismic velocity structure and composition of the
789 continental crust: A global view. *Journal of Geophysical Research: Solid Earth*, 100(B6),
790 9761-9788.

791 Clouzet, P., Masson, Y., & Romanowicz, B. (2018). Box Tomography: first application to the
792 imaging of upper-mantle shear velocity and radial anisotropy structure beneath the North
793 American continent. *Geophysical Journal International*, 213(3), 1849-1875.

794 Colgan, J. P., & Henry, C. D. (2009). Rapid middle Miocene collapse of the Mesozoic orogenic
795 plateau in north-central Nevada. *International Geology Review*, 51(9-11), 920-961.

796 Colgan, J. P., Howard, K. A., Fleck, R. J., & Wooden, J. L. (2010). Rapid middle Miocene
797 extension and unroofing of the southern Ruby Mountains, Nevada. *Tectonics*, 29(6).

798 Compton, R. R., Todd, V. R., Zartman, R. E., & Naeser, C. W. (1977). Oligocene and Miocene
799 metamorphism, folding, and low-angle faulting in northwestern Utah. *Geological Society*
800 *of America Bulletin*, 88(9), 1237-1250.

801 Coney, P. J., & Harms, T. A. (1984). Cordilleran metamorphic core complexes: Cenozoic
802 extensional relics of Mesozoic compression. *Geology*, 12(9), 550-554.

803 Cooper, F. J., Platt, J. P., & Behr, W. M. (2017). Rheological transitions in the middle crust:
804 insights from Cordilleran metamorphic core complexes. *Solid Earth*, 8(1), 199-215.

805 Crampin, S. (1994). The fracture criticality of crustal rocks. *Geophysical Journal International*,
806 118(2), 428-438.

807 Crittenden, M. D., Coney, P. J., Davis, G. H., & Davis, G. H. (Eds.). (1980). *Cordilleran*
808 *metamorphic core complexes* (Vol. 153). Geological Society of America.

809 Dalton, C. A., & Gaherty, J. B. (2013). Seismic anisotropy in the continental crust of
810 northwestern Canada. *Geophysical Journal International*, 193(1), 338-348.

811 Delph, J. R., Levander, A., & Niu, F. (2019). Constraining crustal properties using receiver
812 functions and the autocorrelation of earthquake-generated body waves. *Journal of*
813 *Geophysical Research: Solid Earth*.

814 Dewey, J. F. (1988). Extensional collapse of orogens. *Tectonics*, 7(6), 1123-1139.

815 Dreiling, J., Tilmann, F., Yuan, X., Giese, J., Rindraharisaona, E. J., Rumpker, G., & Wysession,
816 M. E. (2018). Crustal Radial Anisotropy and Linkage to Geodynamic Processes: A Study
817 Based on Seismic Ambient Noise in Southern Madagascar. *Journal of Geophysical*
818 *Research: Solid Earth*, 123(6), 5130-5146.

819 Duret, F., Shapiro, N. M., Cao, Z., Levin, V., Molnar, P., & Roecker, S. (2010). Surface wave
820 dispersion across Tibet: Direct evidence for radial anisotropy in the crust. *Geophysical*
821 *Research Letters*, 37(16).

822 Dziewonski, A. M., & Anderson, D. L. (1981). Preliminary reference Earth model. *Physics of the*
823 *earth and planetary interiors*, 25(4), 297-356.

824 Egger, A. E., Dumitru, T. A., Miller, E. L., Savage, C. F., & Wooden, J. L. (2003). Timing and
825 nature of Tertiary plutonism and extension in the Grouse Creek Mountains, Utah.
826 *International Geology Review*, 45(6), 497-532.

827 Ekström, G., Abers, G. A., & Webb, S. C. (2009). Determination of surface-wave phase
828 velocities across USArray from noise and Aki's spectral formulation. *Geophysical*
829 *Research Letters*, 36(18).

830 Ekström, G. (2017). Short-period surface-wave phase velocities across the conterminous United
831 States. *Physics of the Earth and Planetary Interiors*, 270, 168-175.

832 Erdman, M. E., Hacker, B. R., Zandt, G., & Seward, G. (2013). Seismic anisotropy of the crust:
833 electron-backscatter diffraction measurements from the Basin and Range. *Geophysical*
834 *Journal International*, 195(2), 1211-1229.

835 Feng, L., & Ritzwoller, M. H. (2019). A 3-D shear velocity model of the crust and uppermost
836 mantle beneath Alaska including apparent radial anisotropy. *Journal of Geophysical*
837 *Research: Solid Earth*.

838 Fenneman, N. M. (1917). Physiographic subdivision of the United States. *Proceedings of the*
839 *National Academy of Sciences of the United States of America*, 3(1), 17.

840 Fu, Y. V., & Li, A. (2015). Crustal shear wave velocity and radial anisotropy beneath the Rio
841 Grande rift from ambient noise tomography. *Journal of Geophysical Research: Solid*
842 *Earth*, 120(2), 1005-1019.

843 Gans, P. B. (1987). An open-system, two-layer crustal stretching model for the eastern Great
844 Basin. *Tectonics*, 6(1), 1-12.

845 Gao, C., & Lekić, V. (2018). Consequences of parametrization choices in surface wave
846 inversion: insights from transdimensional Bayesian methods. *Geophysical Journal*
847 *International*, 215(2), 1037-1063.

848 Gébelin, A., Mulch, A., Teyssier, C., Heizler, M., Vennemann, T., & Seaton, N. C. (2011).
849 Oligo-Miocene extensional tectonics and fluid flow across the Northern Snake Range
850 detachment system, Nevada. *Tectonics*, 30(5).

851 Gilbert, H. (2012). Crustal structure and signatures of recent tectonism as influenced by ancient
852 terranes in the western United States. *Geosphere*, 8(1), 141-157.

853 Gorbatov, A., Saygin, E., & Kennett, B. L. N. (2012). Crustal properties from seismic station
854 autocorrelograms. *Geophysical Journal International*, 192(2), 861-870.

855 Hacker, B. R., Ritzwoller, M. H., & Xie, J. (2014). Partially melted, mica-bearing crust in
856 Central Tibet. *Tectonics*, 33(7), 1408-1424.

857 Hacker, B. R., Kelemen, P. B., & Behn, M. D. (2015). Continental lower crust. *Annual Review of*
858 *Earth and Planetary Sciences*, 43, 167-205.

859 Haines, S. H., & van der Pluijm, B. A. (2010). Dating the detachment fault system of the Ruby
860 Mountains, Nevada: Significance for the kinematics of low-angle normal faults.
861 *Tectonics*, 29(4).

862 Hamilton, W., & Myers, W. B. (1966). Cenozoic tectonics of the western United States. *Reviews*
863 *of Geophysics*, 4(4), 509-549.

864 Hammond, W. C., & Thatcher, W. (2004). Contemporary tectonic deformation of the Basin and
865 Range province, western United States: 10 years of observation with the Global
866 Positioning System. *Journal of Geophysical Research: Solid Earth*, 109(B8).

867 Hansen, S. M., Dueker, K., & Schmandt, B. (2015). Thermal classification of lithospheric
868 discontinuities beneath USArray. *Earth and Planetary Science Letters*, 431, 36-47.

869 Harmon, N., & Rychert, C. A. (2015). Seismic imaging of deep crustal melt sills beneath Costa
870 Rica suggests a method for the formation of the Archean continental crust. *Earth and*
871 *Planetary Science Letters*, 430, 140-148.

872 Hasterok, D., & Chapman, D. S. (2007). Continental thermal isostasy: 2. Application to North
873 America. *Journal of Geophysical Research: Solid Earth*, 112(B6).

874 Hastings, W. K. (1970). Monte Carlo sampling methods using Markov chains and their
875 applications.

876 Hauser, E., Potter, C., Hauge, T., Burgess, S., Burtch, S., Mutschler, J., Allmendinger, R.,
877 Brown, L., Kaufman, S., & Oliver, J. (1987). Crustal structure of eastern Nevada from
878 COCORP deep seismic reflection data. *Geological Society of America Bulletin*, 99(6),
879 833-844.

880 Herrmann, R. B. (2013). Computer programs in seismology: An evolving tool for instruction and
881 research. *Seismological Research Letters*, 84(6), 1081-1088.

882 Hodges, K. V., Snoke, A. W., & Hurlow, H. A. (1992). Thermal evolution of a portion of the
883 Sevier hinterland: the northern Ruby Mountains-East Humboldt Range and Wood Hills,
884 northeastern Nevada. *Tectonics*, 11(1), 154-164.

885 Holbrook, W. S., Catchings, R. D., & Jarchow, C. M. (1991). Origins of deep crustal reflections:
886 Implications of coincident seismic refraction and reflection data in Nevada. *Geology*,
887 *19*(2), 175-179.

888 Huang, H., Yao, H., & van der Hilst, R. D. (2010). Radial anisotropy in the crust of SE Tibet and
889 SW China from ambient noise interferometry. *Geophysical Research Letters*, *37*(21).

890 Humphreys, E., Hessler, E., Dueker, K., Farmer, G. L., Erslev, E., & Atwater, T. (2003). How
891 Laramide-age hydration of North American lithosphere by the Farallon slab controlled
892 subsequent activity in the western United States. *International Geology Review*, *45*(7),
893 575-595.

894 Jaxybulatov, K., Shapiro, N. M., Koulakov, I., Mordret, A., Landès, M., & Sens-Schoenfelder,
895 C. (2014). A large magmatic sill complex beneath the Toba caldera. *science*, *346*(6209),
896 617-619.

897 Jiang, C., Schmandt, B., Farrell, J., Lin, F. C., & Ward, K. M. (2018). Seismically anisotropic
898 magma reservoirs underlying silicic calderas. *Geology*, *46*(8), 727-730.

899 Klemperer, S. L., Hauge, T. A., Hauser, E. C., Oliver, J. E., & Potter, C. J. (1986). The Moho in
900 the northern Basin and Range province, Nevada, along the COCORP 40 N seismic-
901 reflection transect. *Geological Society of America Bulletin*, *97*(5), 603-618.

902 Kohlstedt, D. L., Evans, B., & Mackwell, S. J. (1995). Strength of the lithosphere: Constraints
903 imposed by laboratory experiments. *Journal of Geophysical Research: Solid Earth*,
904 *100*(B9), 17587-17602.

905 Konstantinou, A., Strickland, A., Miller, E., Vervoort, J., Fisher, C. M., Wooden, J., & Valley, J.
906 (2013). Synextensional magmatism leading to crustal flow in the Albion–Raft River–
907 Grouse Creek metamorphic core complex, northeastern Basin and Range. *Tectonics*,
908 *32*(5), 1384-1403.

909 Kreemer, C., Blewitt, G., & Klein, E. C. (2014). A geodetic plate motion and Global Strain Rate
910 Model. *Geochemistry, Geophysics, Geosystems*, *15*(10), 3849-3889.

911 Laske, G., Masters, G., Ma, Z., & Pasyanos, M. (2013, April). Update on CRUST1. 0—A 1-
912 degree global model of Earth’s crust. In *Geophys. Res. Abstr* (Vol. 15, p. 2658). Vienna,
913 Austria: EGU General Assembly.

914 Leary, P. C., Crampin, S., & McEvelly, T. V. (1990). Seismic fracture anisotropy in the Earth's
915 crust: An overview. *Journal of Geophysical Research: Solid Earth*, *95*(B7), 11105-
916 11114.

917 Lee, J., Miller, E. L., & Sutter, J. F. (1987). Ductile strain and metamorphism in an extensional
918 tectonic setting: A case study from the northern Snake Range, Nevada, USA. *Geological*
919 *Society, London, Special Publications*, *28*(1), 267-298.

920 Lekić, V., & Fischer, K. M. (2014). Contrasting lithospheric signatures across the western United
921 States revealed by Sp receiver functions. *Earth and Planetary Science Letters*, *402*, 90-
922 98.

923 Levander, A., & Miller, M. S. (2012). Evolutionary aspects of lithosphere discontinuity structure
924 in the western US. *Geochemistry, Geophysics, Geosystems*, *13*(7).

- 925 Lin, F. C., Tsai, V. C., & Schmandt, B. (2014). 3-D crustal structure of the western United
926 States: application of Rayleigh-wave ellipticity extracted from noise cross-correlations.
927 *Geophysical Journal International*, 198(2), 656-670.
- 928 Lin, F. C., Ritzwoller, M. H., Yang, Y., Moschetti, M. P., & Fouch, M. J. (2011). Complex and
929 variable crustal and uppermost mantle seismic anisotropy in the western United States.
930 *Nature Geoscience*, 4(1), 55.
- 931 Lin, F. C., Moschetti, M. P., & Ritzwoller, M. H. (2008). Surface wave tomography of the
932 western United States from ambient seismic noise: Rayleigh and Love wave phase
933 velocity maps. *Geophysical Journal International*, 173(1), 281-298.
- 934 Litherland, M. M., & Klempner, S. L. (2017). Crustal structure of the Ruby Mountains
935 metamorphic core complex, Nevada, from passive seismic imaging. *Geosphere*, 13(5),
936 1506-1523.
- 937 Lloyd, G. E., Butler, R. W., Casey, M., & Mainprice, D. (2009). Mica, deformation fabrics and
938 the seismic properties of the continental crust. *Earth and Planetary Science Letters*,
939 288(1-2), 320-328.
- 940 Long, S. P. (2018). Geometry and magnitude of extension in the Basin and Range Province (39°
941 N), Utah, Nevada, and California, USA: Constraints from a province-scale cross section.
942 *Bulletin*, 131(1-2), 99-119.
- 943 Lowry, A. R., & Pérez-Gussinyé, M. (2011). The role of crustal quartz in controlling Cordilleran
944 deformation. *Nature*, 471(7338), 353.
- 945 Luo, Y., Xu, Y., & Yang, Y. (2013). Crustal radial anisotropy beneath the Dabie orogenic belt
946 from ambient noise tomography. *Geophysical Journal International*, 195(2), 1149-1164.
- 947 Lynner, C., Beck, S. L., Zandt, G., Porritt, R. W., Lin, F. C., & Eilon, Z. C. (2018). Midcrustal
948 deformation in the Central Andes constrained by radial anisotropy. *Journal of*
949 *Geophysical Research: Solid Earth*, 123(6), 4798-4813.
- 950 MacCready, T., Snoke, A. W., Wright, J. E., & Howard, K. A. (1997). Mid-crustal flow during
951 Tertiary extension in the Ruby Mountains core complex, Nevada. *Geological Society of*
952 *America Bulletin*, 109(12), 1576-1594.
- 953 Mahan, K. (2006). Retrograde mica in deep crustal granulites: Implications for crustal seismic
954 anisotropy. *Geophysical research letters*, 33(24).
- 955 Mainprice, D., & Nicolas, A. (1989). Development of shape and lattice preferred orientations:
956 application to the seismic anisotropy of the lower crust. *Journal of Structural Geology*,
957 11(1-2), 175-189.
- 958 Matharu, G., Bostock, M. G., Christensen, N. I., & Tromp, J. (2014). Crustal anisotropy in a
959 subduction zone forearc: Northern Cascadia. *Journal of Geophysical Research: Solid*
960 *Earth*, 119(9), 7058-7078.
- 961 McCarthy, J. (1986). Reflection profiles from the Snake Range metamorphic core complex: A
962 window into the mid-crust. *Reflection seismology: The continental crust*, 14, 281-292.
- 963 McCarthy, J. & Thompson, G. A. (1988). Seismic imaging of extended crust with emphasis on
964 the western United States. *Geological Society of America Bulletin*, 100(9), 1361-1374.

- 965 McQuarrie, N., & Wernicke, B. P. (2005). An animated tectonic reconstruction of southwestern
966 North America since 36 Ma. *Geosphere*, 1(3), 147-172.
- 967 Mikulich, M. J., & Smith, R. B. (1974). Seismic reflection and aeromagnetic surveys of the
968 Great Salt Lake, Utah. *Geological Society of America Bulletin*, 85(6), 991-1002.
- 969 Miller, E. L., Dumitru, T. A., Brown, R. W., & Gans, P. B. (1999). Rapid Miocene slip on the
970 Snake Range–Deep Creek range fault system, east-central Nevada. *Geological Society of
971 America Bulletin*, 111(6), 886-905.
- 972 Moschetti, M. P., Ritzwoller, M. H., Lin, F., & Yang, Y. (2010a). Seismic evidence for
973 widespread western-US deep-crustal deformation caused by extension. *Nature*,
974 464(7290), 885.
- 975 Moschetti, M. P., Ritzwoller, M. H., Lin, F. C., & Yang, Y. (2010b). Crustal shear wave velocity
976 structure of the western United States inferred from ambient seismic noise and
977 earthquake data. *Journal of Geophysical Research: Solid Earth*, 115(B10).
- 978 Mosegaard, K., & Tarantola, A. (1995). Monte Carlo sampling of solutions to inverse problems.
979 *Journal of Geophysical Research: Solid Earth*, 100(B7), 12431-12447.
- 980 Nishizawa, O., & Yoshino, T. (2001). Seismic velocity anisotropy in mica-rich rocks: An
981 inclusion model. *Geophysical Journal International*, 145(1), 19-32.
- 982 Ojo, A. O., Ni, S., & Li, Z. (2017). Crustal radial anisotropy beneath Cameroon from ambient
983 noise tomography. *Tectonophysics*, 696, 37-51.
- 984 Okaya, D., Vel, S. S., Song, W. J., & Johnson, S. E. (2018). Modification of crustal seismic
985 anisotropy by geological structures (“structural geometric anisotropy”). *Geosphere*,
986 15(1), 146-170.
- 987 Panning, M., & Romanowicz, B. (2006). A three-dimensional radially anisotropic model of shear
988 velocity in the whole mantle. *Geophysical Journal International*, 167(1), 361-379.
- 989 Pérouse, E., & Wernicke, B. P. (2017). Spatiotemporal evolution of fault slip rates in deforming
990 continents: The case of the Great Basin region, northern Basin and Range province.
991 *Geosphere*, 13(1), 112-135.
- 992 Platt, J. P., Behr, W. M., & Cooper, F. J. (2015). Metamorphic core complexes: windows into the
993 mechanics and rheology of the crust. *Journal of the Geological Society*, 172(1), 9-27.
- 994 Rahl, J. M., & Skemer, P. (2016). Microstructural evolution and rheology of quartz in a mid-
995 crustal shear zone. *Tectonophysics*, 680, 129-139
- 996 Rey, P. F., Teyssier, C., & Whitney, D. L. (2009a). Extension rates, crustal melting, and core
997 complex dynamics. *Geology*, 37(5), 391-394.
- 998 Rey, P. F., Teyssier, C., & Whitney, D. L. (2009b). The role of partial melting and extensional
999 strain rates in the development of metamorphic core complexes. *Tectonophysics*, 477(3-
1000 4), 135-144.
- 1001 Rey, P., Vanderhaeghe, O., & Teyssier, C. (2001). Gravitational collapse of the continental crust:
1002 definition, regimes and modes. *Tectonophysics*, 342(3-4), 435-449.
- 1003 Rudnick, R. L., & Fountain, D. M. (1995). Nature and composition of the continental crust: a
1004 lower crustal perspective. *Reviews of geophysics*, 33(3), 267-309.

- 1005 Sabra, K. G., Gerstoft, P., Roux, P., Kuperman, W. A., & Fehler, M. C. (2005). Extracting time-
1006 domain Green's function estimates from ambient seismic noise. *Geophysical Research*
1007 *Letters*, 32(3).
- 1008 Schellart, W. P., Stegman, D. R., Farrington, R. J., Freeman, J., & Moresi, L. (2010). Cenozoic
1009 tectonics of western North America controlled by evolving width of Farallon slab.
1010 *Science*, 329(5989), 316-319.
- 1011 Schmandt, B., Lin, F. C., & Karlstrom, K. E. (2015). Distinct crustal isostasy trends east and
1012 west of the Rocky Mountain Front. *Geophysical Research Letters*, 42(23), 10-290.
- 1013 Schmandt, B., Jiang, C., & Farrell, J. (2019). Seismic perspectives from the western US on
1014 magma reservoirs underlying large silicic calderas. *Journal of Volcanology and*
1015 *Geothermal Research*.
- 1016 Schutt, D. L., Lowry, A. R., & Buehler, J. S. (2018). Moho temperature and mobility of lower
1017 crust in the western United States. *Geology*, 46(3), 219-222.
- 1018 Seats, K. J., Lawrence, J. F., & Prieto, G. A. (2012). Improved ambient noise correlation
1019 functions using Welch's method. *Geophysical Journal International*, 188(2), 513-523.
- 1020 Shapiro, N. M., & Campillo, M. (2004). Emergence of broadband Rayleigh waves from
1021 correlations of the ambient seismic noise. *Geophysical Research Letters*, 31(7).
- 1022 Shapiro, N. M., Ritzwoller, M. H., Molnar, P., & Levin, V. (2004). Thinning and flow of Tibetan
1023 crust constrained by seismic anisotropy. *Science*, 305(5681), 233-236.
- 1024 Shen, W., Ritzwoller, M. H., Schulte-Pelkum, V., & Lin, F. C. (2012). Joint inversion of surface
1025 wave dispersion and receiver functions: a Bayesian Monte-Carlo approach. *Geophysical*
1026 *Journal International*, 192(2), 807-836.
- 1027 Shen, W., & Ritzwoller, M. H. (2016). Crustal and uppermost mantle structure beneath the
1028 United States. *Journal of Geophysical Research: Solid Earth*, 121(6), 4306-4342.
- 1029 Sherrington, H. F., Zandt, G., & Frederiksen, A. (2004). Crustal fabric in the Tibetan Plateau
1030 based on waveform inversions for seismic anisotropy parameters. *Journal of Geophysical*
1031 *Research: Solid Earth*, 109(B2).
- 1032 Shirzad, T., & Shomali, Z. H. (2014). Shallow crustal radial anisotropy beneath the Tehran basin
1033 of Iran from seismic ambient noise tomography. *Physics of the Earth and Planetary*
1034 *Interiors*, 231, 16-29.
- 1035 Stipp, M., & Tullis, J. (2003). The recrystallized grain size piezometer for quartz. *Geophysical*
1036 *Research Letters*, 30(21).
- 1037 Stoerzel, A., & Smithson, S. B. (1998). Two-dimensional travel time inversion for the crustal P
1038 and S wave velocity structure of the Ruby Mountains metamorphic core complex, NE
1039 Nevada. *Journal of Geophysical Research: Solid Earth*, 103(B9), 21121-21143.
- 1040 Sullivan, W. A., & Snoke, A. W. (2007). Comparative anatomy of core-complex development in
1041 the northeastern Great Basin, USA. *Rocky Mountain Geology*, 42(1), 1-29.
- 1042 Tatham, D. J., Lloyd, G. E., Butler, R. W. H., & Casey, M. (2008). Amphibole and lower crustal
1043 seismic properties. *Earth and Planetary Science Letters*, 267(1-2), 118-128.

1044 Tesauro, M., Kaban, M. K., Mooney, W. D., & Cloetingh, S. (2014). NACr14: A 3D model for
1045 the crustal structure of the North American Continent. *Tectonophysics*, *631*, 65-86.

1046 Thatcher, W., & Pollitz, F. F. (2008). Temporal evolution of continental lithospheric strength in
1047 actively deforming regions. *GSA TODAY*, *18*(4/5), 4.

1048 Tibuleac, I. M., & von Seggern, D. (2012). Crust-mantle boundary reflectors in Nevada from
1049 ambient seismic noise autocorrelations. *Geophysical Journal International*, *189*(1), 493-
1050 500.

1051 Tirel, C., Brun, J. P., & Burov, E. (2008). Dynamics and structural development of metamorphic
1052 core complexes. *Journal of Geophysical Research: Solid Earth*, *113*(B4).

1053 Tsai, V. C., & Moschetti, M. P. (2010). An explicit relationship between time-domain noise
1054 correlation and spatial autocorrelation (SPAC) results. *Geophysical Journal
1055 International*, *182*(1), 454-460.

1056 Valasek, P. A., Snoke, A. W., Hurich, C. A., & Smithson, S. B. (1989). Nature and origin of
1057 seismic reflection fabric, Ruby-East Humboldt metamorphic core complex, Nevada.
1058 *Tectonics*, *8*(2), 391-415.

1059 Wang, K., Liu, Q., & Yang, Y. (2018, December). Crustal Radial Anisotropy of Southern
1060 California Revealed by Multi-component Ambient Noise Adjoint Tomography. In *AGU
1061 Fall Meeting Abstracts*.

1062 Ward, D., Mahan, K., & Schulte-Pelkum, V. (2012). Roles of quartz and mica in seismic
1063 anisotropy of mylonites. *Geophysical Journal International*, *190*(2), 1123-1134.

1064 Weiss, T., Siegesmund, S., Rabbel, W., Bohlen, T., & Pohl, M. (1999). Seismic velocities and
1065 anisotropy of the lower continental crust: a review. In *Seismic Exploration of the Deep
1066 Continental Crust* (pp. 97-122). Birkhäuser, Basel.

1067 Wells, M. L., Snee, L. W., & Blythe, A. E. (2000). Dating of major normal fault systems using
1068 thermochronology: An example from the Raft River detachment, Basin and Range,
1069 western United States. *Journal of Geophysical Research: Solid Earth*, *105*(B7), 16303-
1070 16327.

1071 Wernicke, B., & Snow, J. K. (1998). Cenozoic tectonism in the central Basin and Range: Motion
1072 of the Sierran-Great Valley block. *International Geology Review*, *40*(5), 403-410.

1073 Wernicke, B., Axen, G. J., & Snow, J. K. (1988). Basin and Range extensional tectonics at the
1074 latitude of Las Vegas, Nevada. *Geological Society of America Bulletin*, *100*(11), 1738-
1075 1757.

1076 Whittington, A. G., Hofmeister, A. M., & Nabelek, P. I. (2009). Temperature-dependent thermal
1077 diffusivity of the Earth's crust and implications for magmatism. *Nature*, *458*(7236), 319-
1078 321.

1079 Whitney, D. L., Teyssier, C., Rey, P., & Buck, W. R. (2013). Continental and oceanic core
1080 complexes. *Bulletin*, *125*(3-4), 273-298.

1081 Wu, G., & Lavier, L. L. (2016). The effects of lower crustal strength and preexisting midcrustal
1082 shear zones on the formation of continental core complexes and low-angle normal faults.
1083 *Tectonics*, *35*(9), 2195-2214.

1084 Wu, G., Lavier, L. L., & Choi, E. (2015). Modes of continental extension in a crustal wedge.
1085 *Earth and Planetary Science Letters*, 421, 89-97.

1086 Xie, J., Ritzwoller, M. H., Shen, W., & Wang, W. (2017). Crustal anisotropy across eastern Tibet
1087 and surroundings modeled as a depth-dependent tilted hexagonally symmetric medium.
1088 *Geophysical Journal International*, 209(1), 466-491.

1089 Xie, J., Ritzwoller, M. H., Brownlee, S. J., & Hacker, B. R. (2015). Inferring the oriented elastic
1090 tensor from surface wave observations: preliminary application across the western United
1091 States. *Geophysical Journal International*, 201(2), 996-1021.

1092 Xie, J., Ritzwoller, M. H., Shen, W., Yang, Y., Zheng, Y., & Zhou, L. (2013). Crustal radial
1093 anisotropy across eastern Tibet and the western Yangtze craton. *Journal of Geophysical
1094 Research: Solid Earth*, 118(8), 4226-4252.

1095 Yuan, H., French, S., Cupillard, P., & Romanowicz, B. (2014). Lithospheric expression of
1096 geological units in central and eastern North America from full waveform tomography.
1097 *Earth and Planetary Science Letters*, 402, 176-186.

1098 Zandt, G., Myers, S. C., & Wallace, T. C. (1995). Crust and mantle structure across the Basin
1099 and Range-Colorado Plateau boundary at 37 N latitude and implications for Cenozoic
1100 extensional mechanism. *Journal of Geophysical Research: Solid Earth*, 100(B6), 10529-
1101 10548.

1102 Zhu, H., Komatitsch, D., & Tromp, J. (2017). Radial anisotropy of the North American upper
1103 mantle based on adjoint tomography with USArray. *Geophysical Journal International*,
1104 211(1), 349-377.